ABSTRACT

Title of Document: Characterization of Electrodeposited Chitosan: an Interfacial Layer for Bio-assembly and Sensing

Susan Buckhout-White, Doctor of Philosophy, 2009

Directed By: Professor Gary W. Rubloff, Department of Materials Science and Engineering and the Institute for Systems Research

Microfluidics and Lab-on-a-Chip devices have revolutionized the field of analytical biology. To fully optimize the potential of the microfluidic environment it is critical to be able to isolate reactions in specific locations within a channel. One solution is found using chitosan, an amine-rich biopolymer with pH responsive solubility. Induction of hydrolysis at patterned electrodes within the fluidic channel provides a means to spatially control the pH, thus enabling biochemical functionalization that is both spatially and temporally programmable.

While chitosan electrodeposition has proven to be reliable at producing films, its growth characteristics are not well understood. *In situ* optical characterization methods of laser reflectivity, fluorescence microscopy and Raman spectroscopy have been employed to understand the growth rate inter diffusion and lateral resolution of the deposition process. These techniques have also been implemented in determining where a molecule bound to an amine site of the polymer is located within the film.

Currently, electrodeposited chitosan films are primarily used for tethering of biomolecules in the recreation of metabolic pathways. Beyond just a biomolecular anchor, chitosan provides a way to incorporate inorganic nanoparticles. These composite structures enable site-specific sensors for the identification of small molecules, an important aspect to many Lab-on-a-Chip applications. New methods for creating spatially localized sites for surface enhanced Raman spectroscopy (SERS) has been developed. These methods have been optimized for particle density and SERS enhancement using TEM and Raman spectroscopy. Through optimization, a viable substrate with retained chitosan amine activity capable of integration into microfluidics has been developed.

CHARACTERIZATION OF ELECTRODEPOSITED CHITOSAN: AN INTERFACIAL LAYER FOR BIO-ASSEMBLY AND SENSING

By

Susan Lynn Buckhout-White

Dissertation submitted to the Faculty of the Graduate School of the
University of Maryland, College Park, in partial fulfillment
of the requirements for the degree of
Doctor of Philosophy
2009

Advisory Committee:

Professor Gary W. Rubloff, Chair

Professor Reza Ghodssi

Professor Robert M. Briber

Professor Oded Rabin

Professor Elisabeth Smela

Dedication

This work is in dedication to all my friends and family who have helped motivate me, stay on task, and remind me why I started on this path. This work is further dedicated to the memory of my Grandmother, Shirley Anne Schaudies, who always reminded me of my potential to succeed.

Acknowledgements

I would like to thank all individuals who have contributed to the development of my research and my research abilities. I would like to thank my advisor, Dr. Gary Rubloff for providing a work environment that encouraged my creativity in science. His guidance has helped me to gain independence and assertiveness in the way I approach research. I would like to thank past group members Drs. Jung Jin Park, and Xiaolong Luo for their guidance and collaboration in the areas of chitosan characterization and microfluidic device development. I would like to acknowledge all Rubloff Group members past and present including Erin Cleveland, Izzy Perez, Dean Berlin, Yi Cheng, Jordan Betz, Parag Banerjee and Lauren Haspert for their helpful discussions and overall support. I would like to thank the Fablab and NISP lab staff as well as my collaborators in the Bentley, Payne and Ghodssi groups.

This work was supported in part by the Deutsch Foundation, the NSF EFRI program, and the FabLab and NispLab facilities in the Maryland NanoCenter.

Table of Contents

List of Tables

List of Figures

Chapter 1 : Introduction

BioMEMS and Lab-on-a-chip technologies have greatly advanced the ability to measure, sense and understand biology quantifiably at the micro scale[1-6], however not all biomolecules can interact with microelectronic surfaces. Often an interface is required to bridge the dissimilar surfaces of biomolecules and traditional microelectronic materials such as silicon and gold. Self assembled monolayers (SAMs), Langmuir-Blodgett films and thiolation[7, 8] have been used commonly for this purpose. Each of these techniques employs chemical selectivity to achieve patterned functionalization. This limits the versatility of the single chip because all of the same surfaces will be functionalized with the same material at the same time, thereby limiting the ability for sequential patterning.

Integrating and manipulating biomolecules to form new nano-bio devices has great promise for biomedical technology, biological and medical science[9], and bio-enabled routes to advanced system applications such as chem-bio detection[10]. Biological nanofabrication has been achieved for biomolecules including antibodies, DNA[11] and viruses[12], using techniques such as microcontact printing[8], and dip-pen lithography[13]. While these techniques achieve high spatial selectivity in the nm range they are limited by the stability of the biomolecules with respect to time and the chemical environments they encounter. In particular, if the patterned biomolecules are utilized in closed systems such as microfluidic arrays, then they must be written on internal surfaces before the bioMEMS chips are completed and sealed for operation.

Thus, it is desirable to create microfluidic systems prior to insertion of biological species, and to add the biology only on demand when the operation is needed (e.g., as a sensor system or biosynthesis chip). The material chitosan offers a unique approach to interfacing the dissimilar microfabricated surfaces while creating locally addressable sites capable of bio-functionalization, because chitosan can be electrodeposited.

1.1 Chitosan Electrodeposition

Chitosan is an amine rich polysaccharide produced from the deaccetylation of chitin, a naturally occurring molecule obtained commonly from the shells of crustaceans[14]. Deacetylation is achieved through exposure with caustic NaOH[14]. The NaOH removes the bound acetyl groups from the chitin. The degree of deacetylation normally varies from 75 to 85%. The molecular weight of chitosan can also vary, but is most commonly used in the range of 100 to 200 kD.

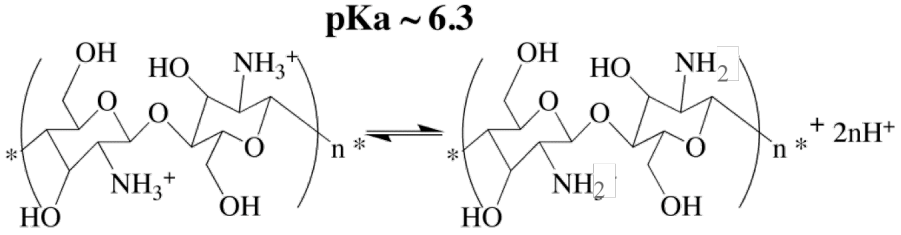

Figure 1.1 Chemical reaction of chitosan at the pH-induced transition

Chitosan allows the interfacing of biology and microelectronics through a reversible pH dependent change in the solubility (Figure 1.1).[15]. The pH change can be produced at the micro scale by inducing an electrochemical reduction of water within the electrolytic chitosan solution[16]. The reduction of water is produced simply through the application of an electric potential across the negatively charged anode in

$$2H_2O + 2e^- \rightarrow 2OH^- + H_2$$

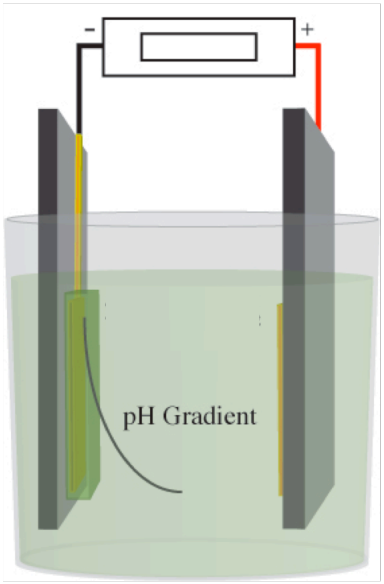

Figure1.2 Schematic of the electrodeposition and the half reaction of water electrolysis at the anode (negatively charged) to produce basic solution

a two-electrode system (Figure1.2). The technique requires the patterning of these two electrodes any place where one functionalized area is desired. However, because multiple electrodes can be addressed individually with respect to time and location, the ability to set up different functionalized areas becomes possible.

1.2 Chitosan Functionalization

The ability to functionalize a surface with chitosan by itself could be useful for passivation, but in conjunction with chitosan's abundantly available amine groups allows for the attachment of biomolecules at any location where an electrode can be patterned. This prevalent chemistry allows for easy attachment of many different types of molecules including, but not limited to DNA, proteins, and enzymes[17-19]. Carboxylic acids and ortho-quinones are specifically reactive with the amine group. The amine group will also form divalent bonds with metals and metal ions allowing

them to bond to metals from solution[20]. By varying when the functionalization occurs in relation to the deposition, molecules can be incorporated into chitosan in three different ways; attachment to deposited chitosan films allows for surface functionalization, attachment to chitosan before deposition allows for volume functionalization, and attachment through the porosity of the chitosan film allows for functionalization through the volume, but in a more patterned method than solution attachment. Electrodeposited chitosan thus exploits heterogeneous bonding and reaction sites as opposed to homogeneous reaction in the liquid or aqueous phase, as depicted in Fig. 1.2.

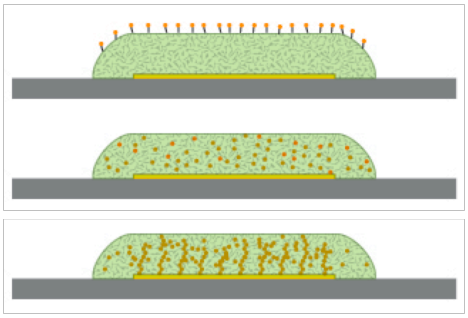

Figure1.3 Schematic of the three different ways to incorporate molecules into chitosan; on top of the pre-formed chitosan film (top), with the chitosan in solution before deposition, and through the porosity of the deposited chitosan.

1.3 Applications to Bacterial Communication

Antibiotic resistance is an increasing health concern. Drugs designed to kill bacteria can lead to gene mutations creating super bugs that are resistant to antibiotics[21]. In order to combat this problem it is necessary to understand how a bacterium behaves and the factors that affect the pathogenicity of the bacteria. Once a bacterium has entered a host, it will secrete an auto-inducer molecule. This molecule is secreted by all the bacteria. When a sufficient concentration of auto-inducer is present the bacterial cell will uptake the molecule, triggering gene

transcription[22, 23], thus initiating an organized response such as biofilm formation or pathogenicity. An alternative approach to fighting bacterial infection is through stopping the creation of the auto-inducer molecule.

One system that is being studied is the enzymatic pathway that produces the quorum sensing molecule auto inducer 2 (AI-2) in escherichia coli (e coli). The pathway that produces this molecule begins with s-adenosylhomocysteine, which interacts with the enzyme PFS and produces adenine and S-ribosylhomocysteine. This in turn interacts with the enzyme LuxS to produce DPD and homocysteine. The DPD undergoes rearrangement and finally forms AI-2. (Figure1.4) [24]. By immobilizing the particular enzymes PFS and LuxS on the chitosan substrate either separately[25, 26] or together [27] in a microfluidic system, we can study the effect that different molecules may have on this pathway.

Figure1.4: AI-2 metabolic reaction pathway[28]

Electrodeposition of chitosan offers an intriguing means to create biochemical reaction sites to duplicate the AI-2 synthesis reaction pathway, providing a strong motivation to pursue the studies at the center of this thesis. Background on techniques of importance for such studies follows in this chapter.

1.4 Fluorescence Microscopy

Fluorescence microscopy is a form of metrology used commonly in the biological sciences. The technique often employs the tagging of the desired target with fluorochromes, small molecules that will emit a specific wavelength of light when excited by a lower specific wavelength, although intrinsically fluorescent molecules are also measured. The fluorescent phenomenon occurs when a photon is excited to a higher orbital through excitation by a specific energy, e.g. by light. When the photon returns to the original state it emits a wavelength of light with less energy (larger wavelength) than the original source. The visualization of this event is commonly observed through excitation with large spectrum light source, such as a Hg lamp, and band pass filters which limit extraneous wavelengths, allowing for the visualization of the often weakly emitted light. It is also possible to excite fluorescence using a single wavelength light source, *ie* a laser), in which case only an emission filter would be needed to block the excitation wavelength. This work uses a Hg lamp and three filters for visualization.

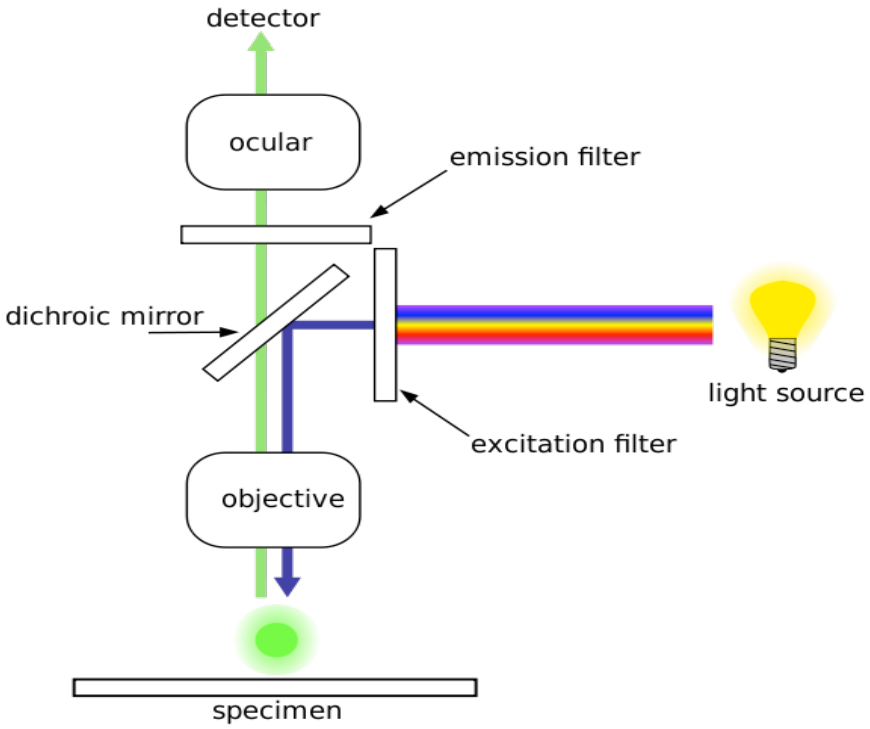

Figure 1.5 Schematic of the optical path for a fluorescence microscope using a broad band excitation source[29]

Three different filters are used in this type of fluorescence microscopy and their optical path is depicted in Figure 1.5. The excitation filter is a narrow band pass that allows only the excitation wavelength to pass. The emission filter is also a band pass filter that allows only the emission wavelength to pass. The third filter is a dichroic beamsplitter that allows for the excitation and emission wavelength to pass through in only one direction, opposite of each other[30].

While qualitative identification of specific molecules is routinely performed using fluorescent microscopy, quantitative fluorescence is more difficult. Variations in quantum yield between different fluorophores and the degrading effects of photo

bleaching limit quantitative fluorescence. Quantification is still possible but care must be taken in maintaining identical conditions between multiple samples.

1.5 Raman Spectroscopy

Raman spectroscopy is a method by which light scatters inelastically with molecular bonds to produce a spectrum with peaks characteristic of specific molecular vibrations. This method of characterization produces peaks similar to those used in infrared (IR) spectroscopy, but in a different manner. IR spectroscopy uses a broad range excitation and identifies molecules based on the wavelength absorbed. Raman spectroscopy uses a signal excitation wavelength and measures the change in wavelength of the scattered light. Both techniques use vibrations characteristic of molecular bonds to identify the overall molecule. The difference between methods, absorption versus scattering, means that a bond that is strong in IR may not be strong in Raman and vice versa. Most importantly for biological samples is that aqueous solutions are measurable in Raman while they are not in IR[31] due to strong absorption of IR by water.

1.6 Surface Enhanced Raman Spectroscopy (SERS)

SERS uses Plasmon resonance to enhance the vibrational output of the Raman signal. A Plasmon is a quantization of the oscillation from an electron cloud produced from the interaction with an electromagnetic excitation[32]. Plasmon resonance is maximized in nanostructures, because the interface between the metal and the surface induces boundary conditions, governed by Maxwell's equations, creating sharp asperities in the produced electromagnetic signal. Noble metals are used to create

these phenomenon because they are easily excited in the visible spectrum. Molecules nearby, within a few Angstroms, will be effected by these strong surface Plasmons leading to the enhancement seen in SERS[31, 33]. There have been many methods demonstrated by others to produce structures with high Plasmon resonance [34-37]. In general there are two ways to produce these structures; naturally formed structures that may or may not use self-ordering and self-assembly, and microfabricated devices that use lithography and thin film processing. The self-formed structures are easier and usually less expensive to form, but are not as ordered and produce less reproducible signal enhancement on the micrometer to millimeter scale. Fabricated structures can offer a more consistent substrate but are much more difficult and time consuming to form. Some of the more sensitive substrates like those made by Liu *et al*[38] are those that combine self-assembly and thin film processes, but these are still difficult to integrate into pre-existing microfabricated devices such as microfluidics.

1.7 Research Goals

The intent of this research is to understand the mechanism by which chitosan electrodeposition occurs so that it may be used to attach and incorporate biomolecules and nanoparticles for assembly and sensing in reconstructed metabolic pathways. To understand the mechanism of deposition, studies are carried out using three different methods of optical characterization. Optical reflectivity, employing a reflected laser beam and a Si detector measure film thickness during growth. Fluorescent microscopy is used to characterize the growth rate of the film, the extent that the film deposits laterally beyond the electrode[39] and the confinement of deposited chitosan

layers. Raman spectroscopy is also be employed for characterization of the lateral growth and depth measurement of bound small molecules.

In order to develop SERS substrates, chitosan is used to mediate the formation of Ag nanoparticles. The optimal films will be developed by varying the deposition methods and concentration of the film precursors. The chitosan/Ag films are characterized using transmission electron microscopy (TEM), electron dispersive spectroscopy (EDS) and image analysis to quantify particle density. The films are formed with the purpose of creating SERS substrates for detection of the small molecule. The SERS enhancement is characterized using Raman spectroscopy.

The understanding of the optimal particle size and shape to maximize the SERS enhancement paired with the understanding of how to produce that size and shape using chitosan allows for the optimal substrate to be developed. Pairing the optimal SERS substrate with knowledge of where molecules bind in chitosan will allow for the future development of a platform that can both assemble enzymes as well as detect their reaction products.

Chapter 2 : Characterization of Electrodeposited Chitosan Growth

2.1 Introduction

Electrodeposition is a reliable means of producing chitosan films on electrodes[19, 40, 41], though thickness and the morphology of the films can vary. It is known that a variety of factors change the resulting film characteristics; chitosan solution concentration, chitosan solution pH, and deposition current density and time[42]. Even when these variables are controlled and tuned, there is still a significant amount of uncertainty in choosing the correct conditions to produce a film of a given thickness. This uncertainty is more apparent when trying to control chitosan deposition to very thin layers.

One approach taken toward understanding the mechanisms that dominate during electrodeposition is *in situ* reflectometry. The instrument is built on the principle that the amount of destructive interference that a laser beam experiences while interacting with the growing chitosan film is directly proportional to the film thickness. The reflectometry has potential for use as a metrology tool to understand the instantaneous growth behavior of the film, or as an advanced process control that would be able to provide feedback when the film has obtained the desired thickness.

A limiting factor in the development of any *in situ* technique designed for measuring chitosan films is that correlation of the data to an existing method is difficult. Chitosan is a hydrogel when it is formed. This characteristic, while highly

desirable for many reasons, causes the film to be very delicate in the hydrated state. The films can be dried, which makes the film suitable for measurement by a variety of techniques. The swollen porous morphology of the film creates a random array of pores that will not collapse uniformly; therefore the dehydrated structure of the film is not necessarily related to the as-deposited film structure. A primary motivation for understanding electrodeposited chitosan films is so they may be more effectively used as a biomolecular interface within microfluidic devices.

One approach to determining *in situ* the as-grown behavior of electrodeposited chitosan is to deposit it in a microfluidic-like chamber. The positioning of an electrode at the top of a PDMS chamber wall will allow the chitosan growth to be visualized in one direction, while maintaining an environment similar to that of the desired application.

2.2 Materials and Methods

Chitosan is prepared from ~ 85% deacetylated chitosan flakes purchased from Sigma. The chitosan is dissolved in 1M HCl and deionized (DI) water until the solution reaches a pH between 2 and 3. The acidic solution is neutralized with 1N NaOH to a final pH of ~5. Additional DI water is added until a 0.5 wt% solution is obtained.

The reflectometer was built using a HeNe laser source, a beamsplitter, an optical chopper, a Si photodetector, and a Gagescope computer-integrated oscilloscope. Figure2.1 illustrates how the instrument was configured.

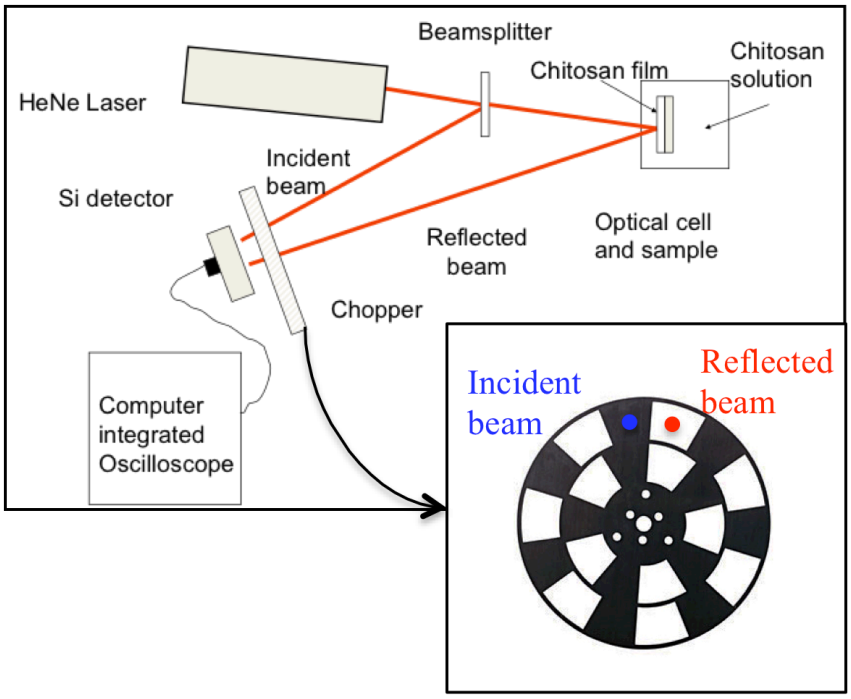

Figure2.1 Schematic of the in-situ reflectivity film apparatus. Inset shows the alignment of the reflected and incident beams with reference to the chopper wheel.

The data obtained outputs as a square wave where each wave plateau is either the incident or reflected beam intensity. Division of these into planes allows for measurement of relative beam intensity. Recorded over time, the relative beam intensity show decreases as the chitosan film is deposited.

The fluorescent chitosan used here was made by reacting N-hydroxysuccinimide (NHS) labeled fluorescein with chitosan. NaOH is added to the chitosan solution to precipitate out a solid gel. The NHS-fluorescein is added to buffer and dimethyl formamide is added to remove the protective group allowing an unstable ortho-quinone to form[43]. This quinone reacts with the amine groups in the chitosan. After reaction, excess fluorescein is rinsed out and the fluorescently tagged chitosan is

redissolved in water to obtain the desired 0.5 wt%. Fluorescent microscopy is performed on a ZEISS LSM 310 microscope. The microscope has been fitted with a Hg lamp and a FITC filter set containing a 470 nm excitation filter, a 495 nm bandpass filter and a 525 nm emission filter.

2.3 Optical Characterization of Film Growth

The reflectometry setup was used to record the *in situ* change in film thickness over a range of deposition times and current densities. The voltage at constant current was simultaneously recorded. When the data is compared (Figure2.2), it is clear that these methods show complementary information. The sharp rise in voltage (Figure2.2a) at the beginning of the deposition indicates that there is a change in the electrical conductivity of the electrode, which gives an indication of deposition, but according to the reflectivity, the thickness is not significantly changed (Figure2.2b). This portion of the data indicates an initiation of the chitosan film growth. As the growth continues, the electrical data plateaus and the reflectivity data show a more linear growth trend. The data in Fig. 2a-2b shows a distinct two or three phase characteristic that implies an initial nucleation with the first few seconds as seen from the electrical data. The reflectivity data show a 30 second region of low loss, indicating a second region, while the third growth region is seen when the reflectivity begins to decrease is a linear manner. After deposition the films are air-dried and measured using a mechanical profiler. The dried film thickness as compared to the endpoint reflectivity shows an overall linear correspondence (Figure2.2c). The endpoint correlation provides an idea of the thickness to expect during deposition.

Because it provides no definite information regarding the wet film thickness, it is not a viable method for characterizing thickness *in situ*.

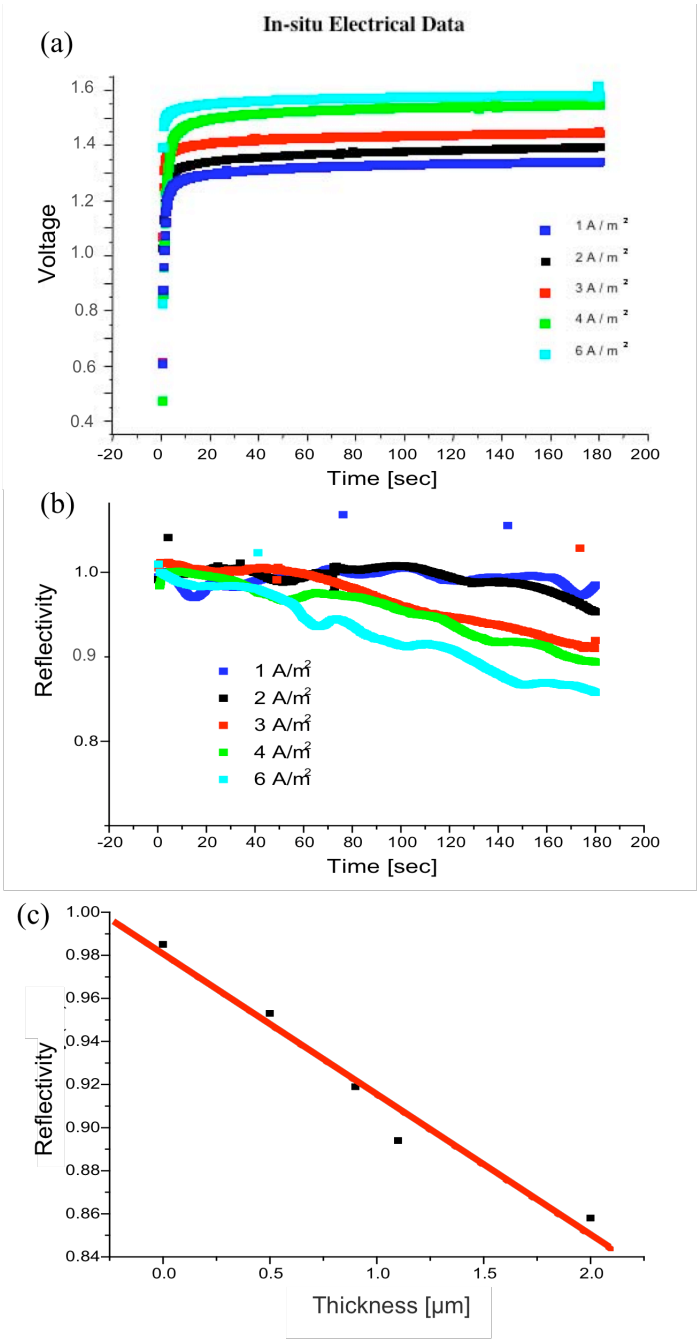

Figure2.2 a)The change in voltage versus deposition time for the given deposition condition. b) The change in *in situ* reflectivity versus deposition time for the given deposition conditions. c) Correlated endpoint reflectivity with post process dry film thickness measurement, linear fit is shown in red.

2.4 Fluorescence Characterization of Film Growth

The ability to characterize chitosan films in a hydrated state has repercussions for the usefulness of the resulting measurement. The simplest way to measure the thickness of the film while it is growing, is to view the electrode in cross-section. Traditional planar electrodes do not have a sufficient thickness to view the step edge of the electrode. Additionally, these electrodes are usually too wide to view end on under a conventional microscope. The demonstrated solution uses a large, ~250 μm^3, PDMS chamber depicted in top view in Fig. 2.3. The chamber is punched with holes large enough to insert tubing for the inlet and outlet as well as 22 AWG .645 mm

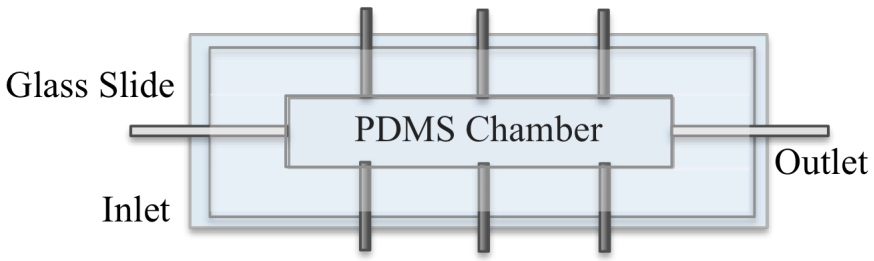

Figure2.3 Scheme of the PDMS deposition chamber for observation of film growth (top view)

diameter wires that serve as the electrodes. The PDMS is permanently sealed to a glass slide using O2 plasma and the wires are inserted after bonding has occurred. The holes punched for the wire are placed adjacent to the chamber ceiling so that growth will be confined to the X and Y directions.

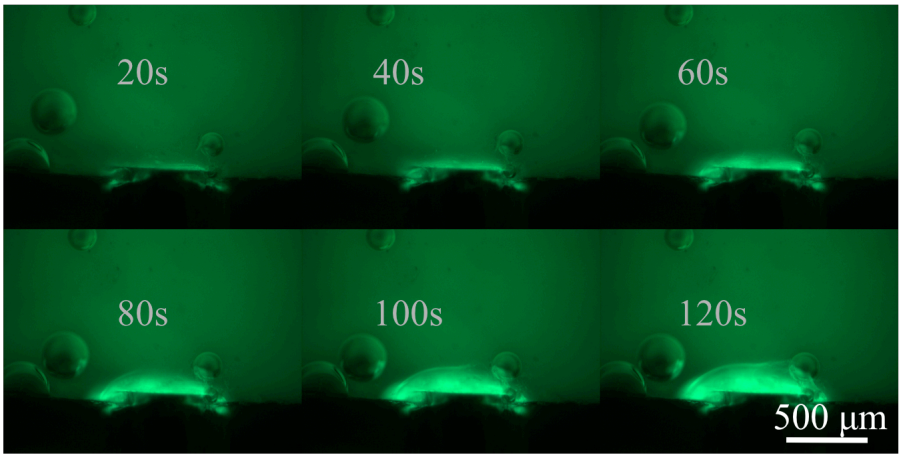

Figure2.4 Time lapse images of chitosan film growth taken every 20 seconds. The images shown are a top down view of one electrode from the device shown in Figure2.3

Fluorescein labeled chitosan solution is used for visualization of the growing film. Figure2.4 shows time lapsed images taken every 20 seconds from the application of an approximately 5 A/m^2 current density. The growth front of the film extends from the wire electrode, the small rectangle extending into the chamber, and continues to the end of the bright fluorescent area. The average thickness along the electrode is determined by measuring the differences between the electrode edge and the chitosan edge at four points. The thickness versus time is plotted in Figure 2.5. It can also be observed that the growth front becomes sharper. This may be due to impingement with the PDMS chamber ceiling.

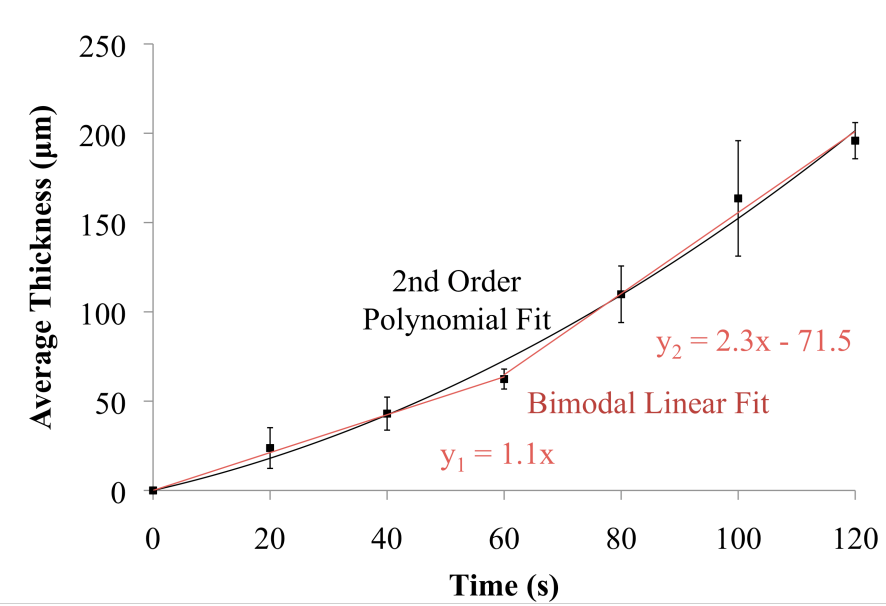

Figure 2.5 Thickness Versus time for the in chamber chitosan growth. The standard deviation of the four points is plotted as error and two types of fits are seen; a bimodal linear fit showing an inflection at 60s, and a 2nd order polynomial

A linear growth rate would be expected from the film, based on the *in situ* reflectometry and post processing thickness data. If the trend is linear, then an inflection exists at 60s, indicating a change in the growth mechanism. The growth rate of the later half of the deposition is about twice that of the first graph. A 2nd order polynomial also fits well to the data, but does not agree with prior observation of a consistent growth rate.

2.6 Conclusion

Measurements of film growth during the deposition process are vital for obtaining information about the mechanism by which chitosan electrodeposits. Both methods for analyzing *in situ* growth shows commonality in the appearance of a slower initial growth region. This slower growth region is the same area that shows the fastest

increase in the electrical response. The reflectometry is less sensitive to measurement anomaly, but must be correlated with an external measure of thickness. The fluorescent chitosan growth is a very simple method that displays growth fronts. Analysis of the images relies on contrast of the fluorescence, which due to the nature of fluorescence, extend beyond the physical edge of the sample. This makes exact measurement of growth rate difficult, but relative growth rates are precise.

The development of these metrologies emphasizes the importance of characterization in the conditions most relevant to the application. While neither characterization method is sufficient in providing all desired information about the growth mechanism, these methods provide far more relevant data than techniques based on dried films.

Chapter 3 : Characterization of Lateral Chitosan Growth

3.1 Introduction

As stated previously, chitosan's unique pH-responsive solubility allows for functionalization of any surface where the pH can locally be raised above 6.3. Figure3.1 illustrates the pH gradient that forms from all electrode surfaces via the hydrolysis of water at the cathode. We have already demonstrated localized, electrically programmable deposition of chitosan and subsequent biomolecular functionalization on the chitosan using microfluidic bioMEMS chips with electrodes 100 to 500 μm in size. Using sequences of aqueous flow and electrode voltages, the creation of localized, biochemically active sites can be programmed within the bioMEMS to achieve biomolecular reaction networks for applications in sensing, synthesis, and drug discovery.

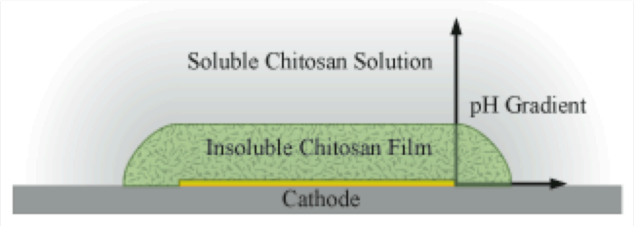

Figure3.1 Schematic of electrodeposited chitosan depicting the pH gradient that forms from all electrode surfaces.

The flexibility of chitosan-based bioMEMS to realize these applications depends in part on how precisely the chitosan can be spatially localized, i.e., the spatial resolution of the electrodeposition process. Previous work has demonstrated deposition on 20 μm electrodes with 100 μm spacing[15], but until now no further work

had been done to determine the limit of the resolution. Here the electrodeposition of chitosan onto metal electrode structures down to a few μm in size is investigated. Fluorescence imaging of deposited, fluorescently labeled chitosan and chemical identification using Raman microscopy both indicate that the chitosan is localized on the electrodes to an edge sharpness of 1 μm or less, suggesting that very small, biologically active sites can be programmed and fabricated within bioMEMS fluidic networks.

3.2 Materials and Methods

Gold electrodes were formed on a passivated 4 inch Si(100) wafer, by deposition of a 5nm Cr adhesion layer followed by 200nm Au. Electrodes were patterned using positive resist and standard optical lithography, with metal etching by Transene Au etch and Cr etchant. Electrodeposition of chitosan was carried out using 0.5 wt% chitosan solution, prepared as described previously[43], after which the wafers were rinsed with DI water. The films were dried before analysis.

For the Raman microscopy studies, 100nm of SiO_2 was used to passivate the Si wafer, on which electrode patterns were formed as 8 mm^2 pads connected by 250 μm wide wires to peripheral contacts. The chitosan was electrodeposited at a constant current of 3 A/m^2 for 120s and measured in a dry state due to weak Raman signal from the hydrated film. The Raman microscopy was performed on a Jobin Yvon LabRamHR Raman microscope enabled with a motorized x-y control and a piezo z control. The scans were performed using a HeNe laser (633 nm), a 600 line grating, a 250 μm entrance aperture size with a 100 μm slit, and a 100× objective lens. The spot

size at the sample for this magnification is 1 μm in diameter and has an approximate sampling depth of 2 μm. The scans were taken in both acquisition and mapping modes at a 4s integration time with averaging over 4 scans.

For the fluorescence microscopy studies, a Si_3N_4 passivated Si wafer was used. Chitosan was prepared by conjugating with NHS-fluorescein to achieve fluorescence microscopy of the deposited chitosan area. Fluorescence microscopy was performed on the Zeiss LSM 310 microscope with the FITC filter set. Electrode patterns consisted of a variety of line widths from 1 μm to 50 μm with varying geometries including corners and curves, connected to larger contact electrodes 250 μm in size. While our previous work has shown constant current mode to be preferred for the chitosan electrodeposition[15], we used constant voltage mode (2.1 V, 10 min) for the fine line patterns to be imaged in fluorescence in order to compensate for significant fluctuations in the effective electrode area as solution level varied along the wire. The resulting fluorescence images were analyzed using ImageJ software provided free by the National Institutes of Health.

3.3 Fluorescent Microscopy Study

Spatial localization of the electrodeposited chitosan was also evaluated using electrode test patterns as shown by the bright field optical micrograph in Figure3.2. These Au electrode patterns included wires from 1 μm to 20 μm in width connected to external contact pads by wires 250 μm in width. Patterns included rectangular and curved geometries. As described above, electrodeposition was carried out as in Figure3.1 using chitosan labeled with NHS-fluorescein to allow fluorescence

microscopy of the lateral extent of the chitosan. Resulting fluorescence micrographs are shown in Figure3.2c and 3.2d for rectangular and curved corner structures respectively. In contrast, the control in Figure3.2b involved exposure to the same fluorescently labeled chitosan solution, but with no voltage applied to the electrode, and as expected the absence of fluorescence indicates that no deposition occurred.

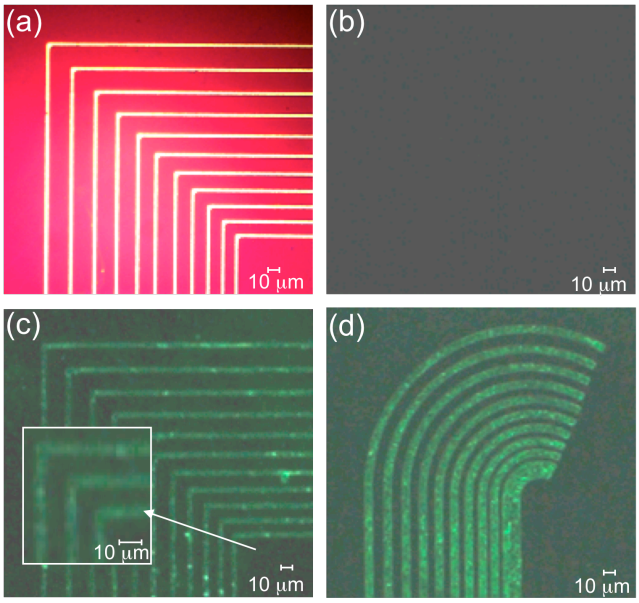

Figure3.2 Micrographs for test structures. (a) Bright field optical micrograph of Au electrodes before chitosan electrodeposition for 2 µm linewidth rectangular test pattern. (b) Fluorescence micrograph corresponding to (a) after immersion in chitosan without an electric field applied, i.e. as a control. (c) Fluorescence micrograph for test pattern in (a) after immersion in chitosan solution and electrodeposition. (d) Fluorescence micrograph for a curved geometry pattern under electrodeposition conditions like those in (c).

Several results are apparent from Figure3.2. First, the electrodeposition produces fluorescent chitosan at the electrodes in similar shapes and sizes as that of the original Au electrodes, suggesting that the chitosan features can be controlled to a few µm. Second, this ability to pattern chitosan as a biomolecular platform is retained in different geometries, illustrated by the rectangular and curved patterns in Figure3.2c

and 3.2d, respectively. Third, there is significant non-uniformity in the fluorescence intensity, suggesting that the electrodeposition process is not spatially uniform on a microscopic length scale, and particularly on the scale of the electrode features of interest for bioMEMS application. This suggests that the electrodeposition process involves nonlinear and/or defect-related behavior. For example, a likely possibility is that while the initial deposition is stochastic, subsequent deposition decorates and is preferentially enhanced where chitosan is already present. This could happen if the initial chitosan modifies local electric fields and pH gradients to alter the spatial distribution of further deposition.

We have analyzed both the bright field and fluorescence micrographs using ImageJ software to process the captured digital images. Image maps corresponding to the fluorescence micrographs of Figures 3.2c and 3.2d are presented in surface plots in Figures 3.3a and 3.3b, respectively. The variability in intensity along the lines underscores the non-uniformity of fluorescence from the electrodeposited chitosan. The short peak of intensity in between the fluorescent lines illustrates the small amount on fluorescent chitosan residue that is attached to the substrate.

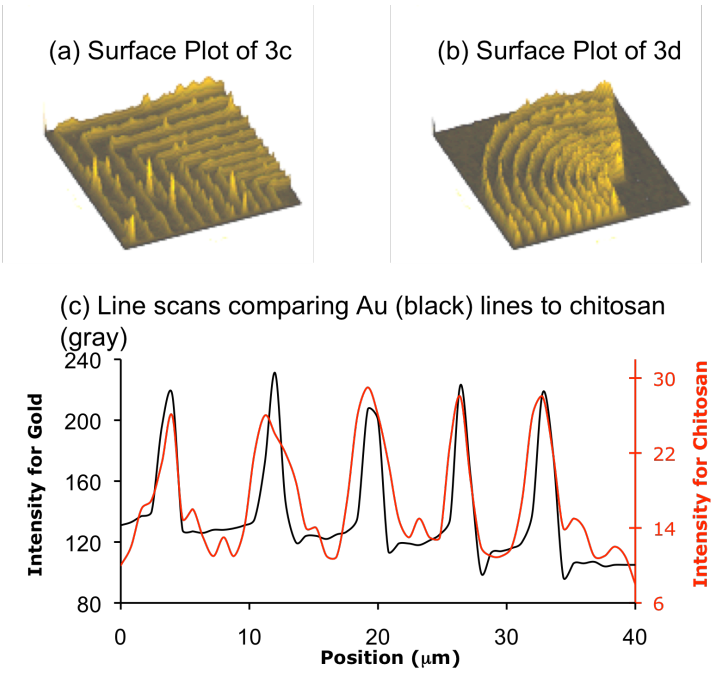

Figure3.3 Image analysis results for rectangular and curved electrode patterns (using ImageJ analysis software): (a) and (b) depict fluorescence intensity maps corresponding to Figs. 3c and 3d respectively, revealing micro-scale non uniformities in chitosan thickness; (c) compares a bright field line scan for Au electrode to a fluorescence line scan for the chitosan layer, showing broadening of the chitosan profile compared to the initial electrode line width.

To assess lateral broadening of the pattern due to chitosan electrodeposition, we have analyzed representative regions of the surface plots using ImageJ software to generate intensity line scans across the electrodes. An example is shown in Figure 3.3c, comparing fluorescence line scans for the chitosan to corresponding bright field line scans for the initial Au electrode. Modest broadening of the chitosan patterns for the profiles of the original Au electrodes is apparent: the Au patterns shows a full-width at half-maximum (fwhm) averaging 1.6 μm, while the chitosan patterns shows a larger fwhm of 2.6 μm, i.e. about 1.0 μm larger, or 0.5 μm per edge. This is consistent with the Raman results (Table 3.1), which showed about 0.8 μm shift of the chitosan edge profile.

3.4 Raman Microscopy Study

Since the motivation for use of electrodeposited chitosan is to control the spatial localization of biochemical functionality arising from biomolecular conjugation to chitosan's amine groups, direct chemical measurement of the chitosan on the electrode is desirable. For these studies we used large, 1 mm X 8 mm, electrodes consistent with the size scale used for microfluidic experiments. Figures 3.4a and 3.4b show the Raman signals from the chitosan film and the Si substrate. Figure 3.4c shows an expanded micrograph of the image of the electrode edge and indicates by the dashed box the region that was scanned.

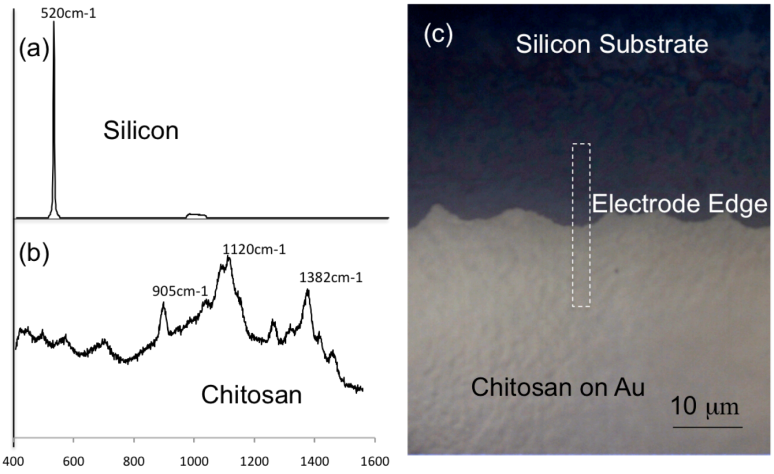

Figure3.4 (a) and (b) indicate the expected peaks for the Si and chitosan spectrum. (c) Micrograph of the electrodeposited chitosan on the Au edge with the dashed box outlining the area that was mapped. (Gold edge is rough from exposure using plastic transparency mask).

To allow for systematic study of the chitosan/Si interface, an x-y Raman map was obtained. The map covers a region of 2 μm across a length of 18 μm. The edge roughness of the electrode edge is a result of lithography through a plastic transparency mask; however, the size scale of the roughness is larger than the scan

size for the Raman mapping and therefore has no effect on the results. Raman spectra were measured every 0.5 μm in both the x and y direction. Two key Raman shifts, 520 cm^{-1} for Si and 1382 cm^{-1} for chitosan, were chosen and subsequently their intensities were plotted as a function of position. It is important to note that while SiO_2 is present it is sufficiently thin and the signal of the primary Si peak is sufficiently strong that this does not affect our results. A plot was produced by assigning a grayscale value to the intensity of the designated peak. This process assigns the maximum value of 256 to the most intense peak, while the system zero is assigned to the 0 value. All intensity values are proportionally assigned a value based on this scale. This produces an image with the grayscale intensity directly proportional to the given signal intensity. The grayscale intensity is then plotted as a function of the distance from the chitosan/Si interface in Figures 3.5a and 3.5b with the grayscale image shown above the plot. A comparison wafer with Au patterns on Si but without any chitosan deposition was scanned over an identical region, and the intensity of the grayscale image was plotted with respect the distance from the interface, shown in Figure 3.5c. This plot produces an experimental means for examining the spatial resolution of the Raman instrument.

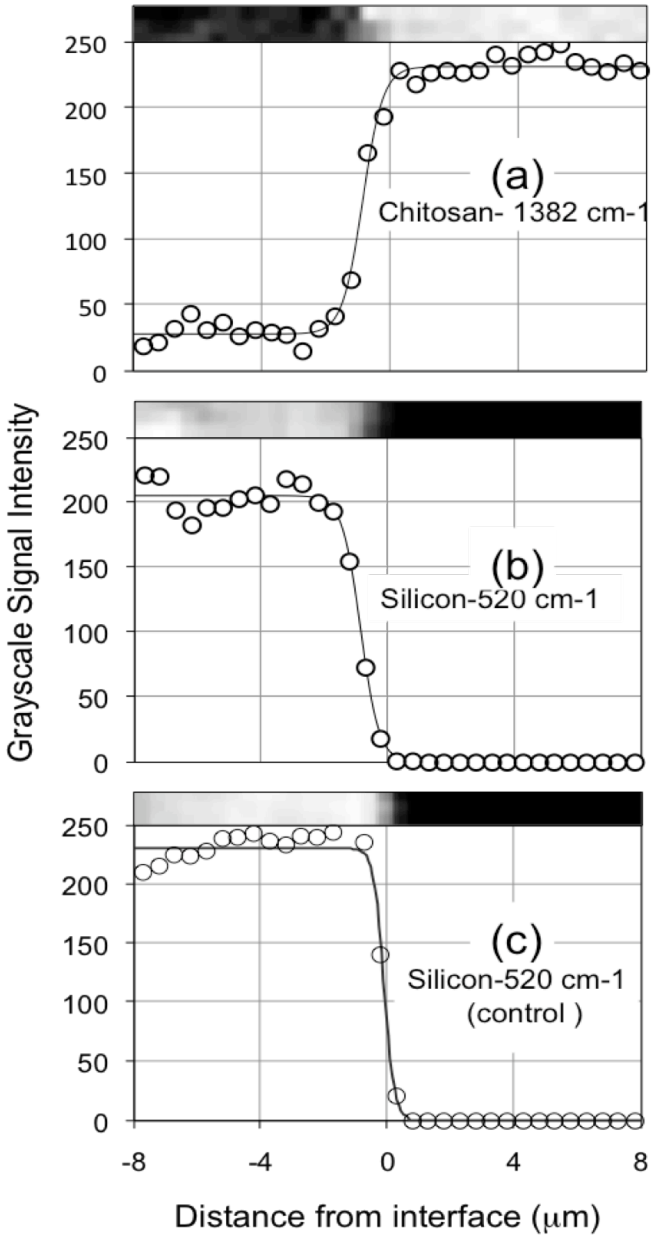

Figure3.5 Raman intensity profiles across the edge of chitosan electrodeposited on patterned Au electrodes on Si wafer for (a) the chitosan, (b) the uncovered Si region, and (c) the Si exposed next to Au electrode without chitosan deposition (as a control). Grayscale images, shown above each plot, are the source from which average Raman intensities were derived (data points) as a function of distance across the chitosan/electrode edge and then fit via regression (solid curves) with a sigmoidal function.

The sampling region for the Raman microscopy measurements is 1 μm in diameter, determined by the laser focus through the microscope. To estimate the spatial localization of the electrodeposited chitosan film, the Raman intensity data in Figure 3.4 were fit using a sigmoidal regression, shown by the smooth curves through the data points in Figures 3.5a-c. The Raman profiles for the control (Fig. 3.5c) are clearly sharper than those for the chitosan edge (Figure 3.5a) and uncovered Si next to the chitosan edge (Figure 3.5b), showing that the electrodeposition of chitosan produces a broadened edge definition. In addition, the chitosan edge is shifted laterally beyond the Au electrode, indicating that the electrodeposition process is three-dimensional. This is not surprising given the fact that the deposition occurs through local pH gradients caused by the electric field and associated hydrolysis, and noting that the field extends laterally from the Au electrode edge.

Analyses of these curves indicate the position of the chitosan edge relative to the underlying Au/Si interface, as well as the broadening of the chitosan edge. The analysis is performed analytically by determining the x values which correspond to one standard deviation of the y value, i.e., 34% above and below the mean. The positions for $+1\sigma$ and -1σ are subtracted to determine the breadth of the chitosan edge, while the position where the Raman intensity reaches half its maximum value is considered as the position of the edge. Table 3.1 shows these values for the chitosan (a) where chitosan was electrodeposited, the Si uncovered by chitosan (b), in comparison to the Si control (c) at the Au/Si interface without chitosan present.

Table 3.1 Positions of electrodeposited chitosan edge vs. Au/Si interface as extracted from sigmoidal fits (Fig. 2) at one standard deviation from the position of the Raman intensity midpoint (considered as the interface). From this a relative interface width is determined as the difference between the +1σ and −1σ positions

Value in μm	Chitosan	Si (experimental)	Si (control)
-1σ	-1.36	-1.36	-0.40
+1σ	-0.34	-0.40	0.14
Interface Width	1.02	0.95	0.54
Interface Position	-0.85	-0.88	-0.13

Table 3.1 shows agreement between the chitosan and Si Raman profiles in determining the position and width of the chitosan edge. The chitosan edge is shifted about 0.75 μm, experimental minus control, from the original Au electrode edge over the Si, a consequence of the lateral growth component. This also indicates that the thickness of the chitosan at the interface is sufficient to dominate the trends of both the chitosan and Si chemical signatures. Comparison to the control reveals a 2X edge broadening between the experiment and the control, illustrating that there is a gradient in the thickness of the chitosan at the edge of the electrode, which would be expected for a field-defined growth mechanism. As the chitosan becomes thin enough the Raman signal of the underlying Si is no longer shielded and therefore a strong Si peak is present.

3.5 Discussion

The results demonstrate that the electrodeposition of chitosan can be accomplished with spatial resolution in the range of 1 μm or less. This localization has been shown in both fluorescence microscopy of the electrodeposited chitosan material and in Raman chemical signatures for the presence/absence of chitosan. The spatial resolution defines a controllable dimensionality about 20X smaller than that reported in prior work[43]. More importantly, it demonstrates that the biomolecular binding capability of chitosan, a consequence of its amine-rich structure, can be harnessed in structures whose dimensions are well below those used in microfluidic networks, thus enabling the use of programmable chitosan reaction sites in bioMEMS networks for a variety of applications.

As described in Figure 3.1, the mechanism for electrodeposition of chitosan is the creation of a pH gradient and elevated pH at the negative electrode, cf. acidic pH in the bulk of the solution. This gradient is mainly caused by the continuous hydrolysis of water, consistent with electrochemistry studies.[16] While the charge state of chitosan's amine groups may also play a role, the extent of this contribution is not yet understood. The primary mechanism is that the elevated pH causes chitosan in the vicinity of the negative electrode to become insoluble, thus resulting in plating-out of solution and deposition or precipitation on the electrode. This mechanism can form relatively thick films, even to the mm regime. The microstructure of the resulting chitosan film can vary between a hydrogel and a more compact film[44], depending on the specific process conditions.

At the edge of the negative electrode, one would expect fringing electric fields to cause elevated pH laterally disposed from the electrode, as well as vertically above it. Thus it is not surprising to observe lateral growth of the chitosan layer from the underlying Au electrode pattern, as seen in the fluorescence micrographs in Figure3.5 and underscored by the image analysis comparison of chitosan and Au line shapes in Figure3.2. It is interesting to note that while the thickness of these films were not measured, the lateral extent is between 50 and 100% of measured thickness from films deposited at the same condition, ~1 μm. Though the Raman results involved larger structures and thus do not provide corresponding line scans across narrow electrode structures, one would expect Raman investigations on narrow electrode structures to be consistent with the line scan results obtained from fluorescence and bright field imaging.

These results indicate edge broadening of 0.5 to 1.0 μm for chitosan electrodeposition on well-defined electrodes, an important practical conclusion for bioMEMS designs exploiting chitosan as a biomolecular platform. While the mechanism of chitosan electrodeposition – local pH gradients – is fully consistent with these results, detailed modeling of the local fields and resulting pH gradients is yet to be addressed. Even more challenging is to understand the role of already-deposited chitosan material on subsequent electric field distributions and conductivity on further deposition, which may contribute to the non-uniformities observed. Even without this level of theoretical understanding, the conclusion that chitosan electrodeposition involves minimal lateral broadening (0.5 to 1.0 μm from electrode

edges) is a significant practical result for application of chitosan biomolecular platforms in bioMEMS.

3.6 Conclusions

As a versatile platform for programmable biomolecule assembly and applications in bioMEMS, the patterning capability of electrodeposited chitosan determines the design flexibility for its use in these applications. This work demonstrates that chitosan electrodeposition replicates electrode features used to localize it to within 0.5 to 1.0 μm from electrode edges, based on both chemical identification of the chitosan through Raman microscopy and also bright field and fluorescence microscopy comparisons of initial electrode patterns and subsequent chitosan overlayer patterns. This modest broadening of chitosan features laterally to the deposition electrode is consistent with current understanding of the electrodeposition mechanism: elevated pH is generated by hydrolysis of water near the negative electrode, extending laterally as well as vertically, and this gradient renders the chitosan insoluble, leading to deposition. With bioMEMS applications that employ electrodeposited chitosan in a thickness regime of order 1 μm therefore, lateral definition of the electrically programmable, biologically active chitosan sites can be achieved on length scales considerably smaller than the dimensions of microfluidic systems, where flow channels in the range 30 to 500 μm are common.

Chapter 4 : Characterization of Chitosan Depth Confinement

4.1 Introduction

Analysis of chitosan growth, both *in situ* visualization and post processing characterization, only provides information on how the film behaves as a whole. This type of metrology does not give insight into how the molecule interacts with the growing hydrogel film during its formation, nor diffusion and permeation mechanisms for chitosan monomers or other species within the film. When chitosan is depositing, it is possible that a new layer forms on the surface, in a step-wise growth pattern. It is also possible that the electrodeposition causes the chitosan to grow into the film as well as out from the surface. It is not assumed that the chitosan will deposit new film at the electrode surface, as the already deposited film will impede diffusion, but some inward diffusion would not be unexpected. Film deposition behavior can be tested by depositing chitosan that has two distinct labels, most conveniently provided by fluorescence labeling. As such methods are well established and pervasively used in biology, differently-labeled chitosan species can be regarded as chitosan "isomorphs" that can be deposited sequentially. If the process mechanism is layer-by-layer overgrowth, then the subsequent chitosan will reside on top of already-deposited chitosan. Examination of the size of the two layers will indicate how much overlap is present. If the chitosan stays well confined it is possible that this technique may be applicable for depositing embedded layers.

As important as it is to understand how chitosan interacts with itself, it is equally important to understand how binding species interact with the chitosan film. An important aspect to utilizing this material as an anchor is understanding where the attachment takes place. Chitosan's hydrogel morphology makes it unclear which portion of the film is interacting with the binding species. Three scenarios exist; the interface region between binding species and chitosan is truly at the geometric surface of the film; the interface is at the effective surface of the film, the surface which accounts for additional area contributed from surface roughness; or the interface is through the entire film, that is the pore structure is sufficiently large so that the entire volume of the film is effectively the surface. Chitosan films deposited at different current densities, but at the same time, should have different microstructures and different thicknesses[42]. Films deposited at the same current density, but for different times, will only show a difference in thickness. Analysis of the quantity of bound molecules to chitosan films in these two different scenarios will indicate whether the molecules are surface or volume bound, and whether the current density has an effect of the amount of molecule bound.

The location of the binding species may not only be related to the film either. The structure of the film most likely has a critical dimension of porosity, which will control permeation and diffusion through the wet film. This means that a binding molecule smaller than this dimension will attach throughout the film, while a molecule larger than the critical dimension will only attach to the surface. It is therefore necessary to test binding molecules of different sizes to determine what this critical dimension is.

4.2 Materials and Methods

The fluorescent layer experiment was carried out in the same chamber at the fluorescent growth from Chapter 2. Two kinds of fluorescently tagged chitosan solution are used, NHS-fluorescein and NHS-Rhodamine. Both chitosan solutions were prepared in the same manner as described in 2.2. Analysis was performed on the LSM 310 microscope using both FITC and TRITC filter sets. The TRITC filter set has an excitation filter of 535nm and an emission filter of 610nm. The bandpass filter is 565nm. Image analysis was done using Image J software.

The quantification of the fluorescein was performed on the JY LAbRam HR as described in 3.2. The scans were taken at 3s integration time with 10 averages. The confocal hole was set to 500nm with a spectrometer slit of 100nm. No filter used for this experiment.

4.3 Confinement of Chitosan Layers

Visualization of a layered hydrogel film is inherently difficult. When measuring the growth fronts of a depositing chitosan layer it is helpful to isolate the z growth direction. In the PDMS chamber this is done by placing the wire electrode in the sidewall at the top, so that it is in contact with the chamber ceiling. This contact prevents growth toward the microscope, which affects the focus depth for viewing the edge. If perfect contact is not achieved, adjustment of the focus depth can alleviate these issues. When considering a two-step deposition, this concern is even more crucial for obtaining relevant data. Fluorescence microscopy of the chitosan hydrogel will detect both layers, even if they are on top of each other, but without a defined

growth start there is no way to determine whether the second layer is diffusing into the first layer or if the two layers are simply both present.

The experiment is conducted by flowing fluorescein labeled chitosan, F-chitosan, into the PDMS chamber. The potential is applied to the electrodes at a current density of ~5 A/m^2. In this case the exact area of the electrode is difficult to determine. The flat surface area of the end of the wire can be calculated, but additional area contribution can be added if the electrode end is not flat. The potential is applied for 2 minutes and an image is captured every 20 seconds using the FITC filter set. Once the deposition is finished, the potential is removed. The acidic chitosan solution must also be removed using reverse pressure, otherwise it will begin to dissolve the deposited film. A new phosphate buffer must then be introduced to prevent film drying. In these cases it is necessary to use a buffer, as DI water that has been exposed to air is usually slightly acidic and would also begin to dissolve the film. Once the film is rinsed, rhodamine labeled chitosan, R-chitosan, is introduced into the channel. The same current is applied and the deposition proceeds for 2 minutes, with images captured every 20 seconds using the TRITC filter set. After deposition the chitosan is again removed and rinsed.

Comparison of the images from the end of each of the separate deposition steps provides information regarding how the chitosan molecule interacts with itself during deposition. Figure4.1 shows the end points of each stage of the 2-stage process. The third image is digitally layered, using Image J, by taking the maximum values from each of the scans and superimposing the values on top of one another.

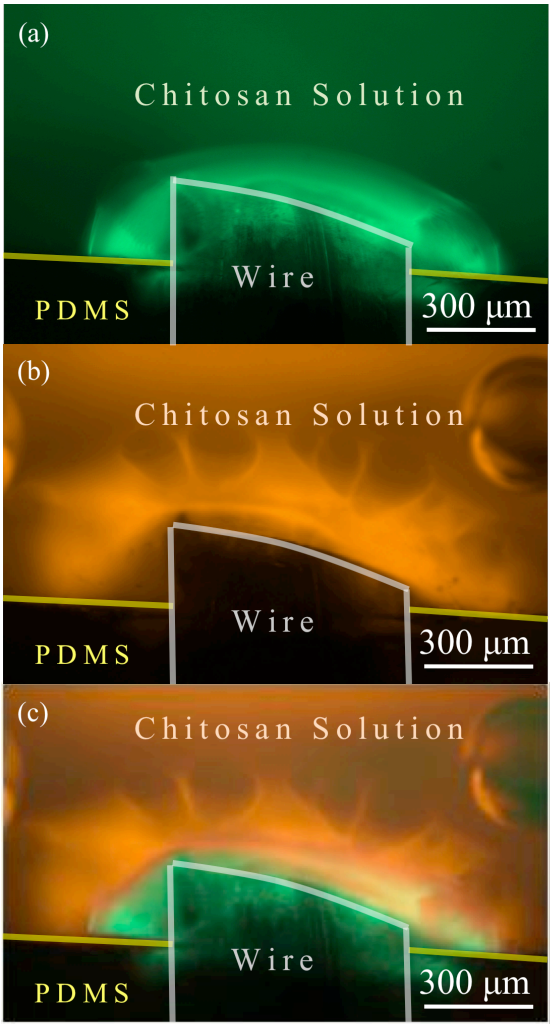

Figure4.1 Chitosan deposition onto a wire, 645 µm in diameter in a PDMS chamber. a) Fluorescein labeled chitosan deposited onto bare wire. b) Rhodamine labeled chitosan deposited after deposition of fluorescein labeled chitosan c) Superimposition of the two images indicating where there is overlap in the layers

Analysis of the first image shows fairly uniform growth from the wire surface. It is clear from this image that the wire is not in full contact with the PDMS chamber ceiling at the point where the wire is inserted through the PDMS, because the fluorescent color can be seen on top of the wire as well as slightly inside the PDMS chamber edge. Analysis of the R-chitosan image (4.1b) shows the growth of the R-

chitosan coming off a slightly darker area surrounding the electrode. Based on the shape of the film in Figure4.1a, it can be assumed that this dark region is the first deposition layer, i.e. fluorescein-labeled chitosan. This image alone demonstrates that to some extent the electrodeposited chitosan grows in discrete layers.

Figure4.1c, the film after each growth layer, superimposed, indicates that there may be some overlap at the edge of the two layers. Some overlap of the read and green color is present in Figure4.1c. The figure also shows a darker region surrounding the deposited film. This may be an artifact of the imaging process, or it may be that there is some depletion of the chitosan from solution directly surrounding where the chitosan forms.

Two explanations for the overlapping interface seen in Figure4.1 can be (1) interdiffusion of the two layers, or (2) that introduction of the second chitosan solution and subsequent deposition dissolves a portion of the original film. This can be investigated by comparing fluorescent micrographs of the film after the first deposition and second deposition both using the FITC filter set. Figure4.2 shows the film at these two stages. The edges of the films after the second deposition step

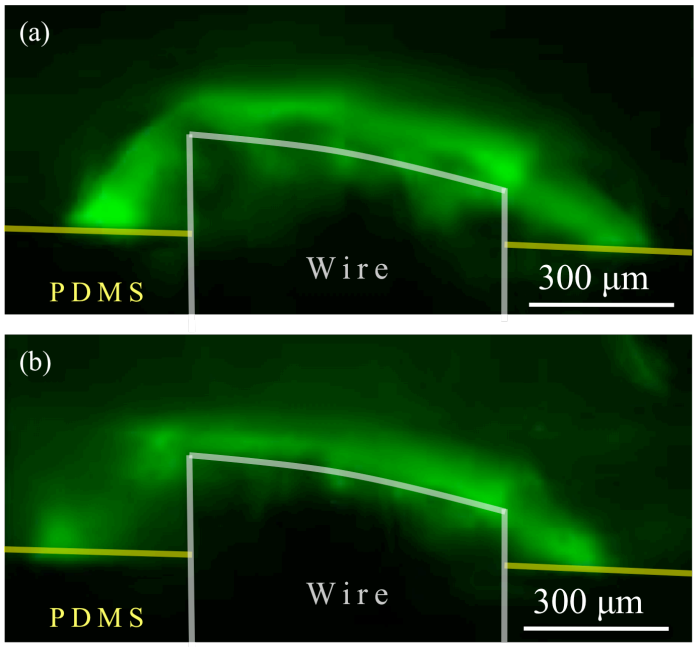

Figure4.2 Fluorescent micrograph of chitosan through the FITC filter set. a) Layer one of the fluorescein labeled chitosan, rinsed, after the first deposition. b) Layer one of the fluorescein labeled chitosan after the rhodamine has been deposited on top.

are less defined compared with the first deposition step. The chitosan that can be seen on top of the electrode is also less after the second stage. Figure4.2 indicates that the overlapping edges seen in Figure4.1 is due to dissolution that occurs at the interface between the depositing layer and the existing film. It is unclear whether this is more noticeable because of the two discrete stages, but the effect of dissolution of films in the chitosan solution is expected since the solution is at a pH of 5, less than the p_{Ka} of 6.3.

4.4 Confinement of Attached Fluorescent Molecules

Understanding where an attached species binds within the chitosan film requires either precise spatial selective chemical identification or quantification of the amount

of bound species, and knowledge of the approximate surface area and volume of the chitosan film. Fluorescent tagging is an easy method for detecting the presence of a molecule. Attachment of NHS-fluorescein to the chitosan amine groups has been reported many times and is an ideal small molecule model system. Quantification of fluorescent molecules, while possible, is difficult since the quantum yield calculation would require knowing the number of amine groups present in the film. The fluorescein molecule is identifiable using Raman spectroscopy. Combining the well understood binding mechanism of NHS fluorescein attachment with quantification and spatial resolution of Raman spectroscopy allows for a straight forward approach to determining the amount of fluorescein bound.

Even though quantification is possible using Raman spectroscopy, it involves correlation to standard concentration measurements. Determining the location of the molecule can be done using a ratio of the fluorescein peak to the chitosan peak and should provide information as to whether the peak is the same relative strength as the chitosan, volume bound, or if it is relatively less intense than the chitosan, surface bound. Since the relative intensities of the two peaks are not identical, a series of samples at different thicknesses will provide a reference for determining the location of the fluorescein. Specifically the use of three different current densities deposited at the same time will provide three samples of varying thicknesses. It is also possible that these films may be of different roughness, which could also affect the binding location. Therefore a fourth sample taken at a duplicate current density, but for a longer time, will provide a sample of varied thickness, but controlled roughness. The Raman spectrum is mapped over 12 points and the average intensities of the

fluorescein 1312 cm^{-1} peak is compared to the chitosan 1370 cm^{-1} peak (Figure4.3a). If the ratio of the two peaks is constant, then the fluorescein is bound throughout the volume of the film. If the ratio increases with decreasing current density and thickness, the molecule is surface bound. Figure4.3b shows a plot of the average ratio for the films. The error bars plotted are the standard deviation of the data.

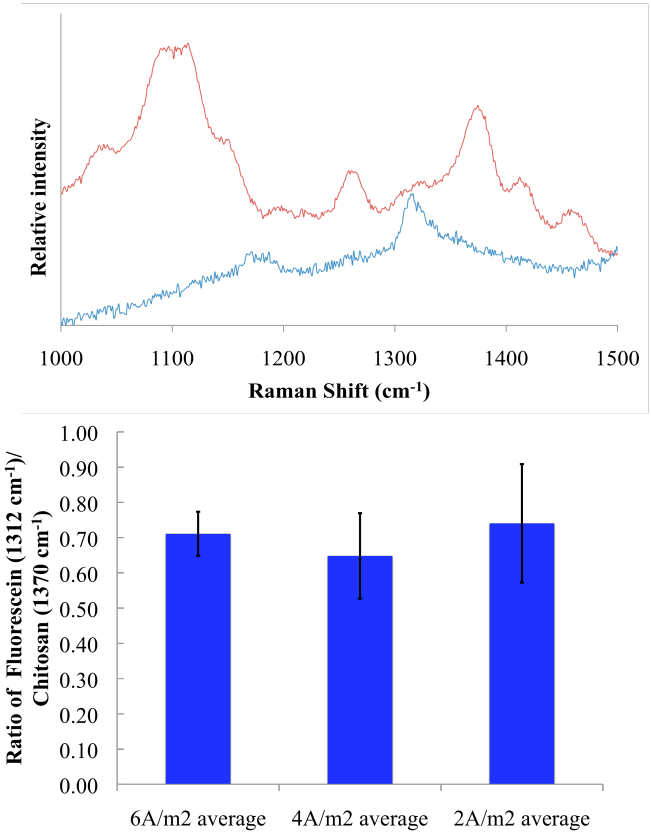

Figure4.3 Raman spectra of chitosan and fluorescein free acid (top). Ratio of the fluorescein 1312 cm^{-1} shift to the chitosan 1370 cm^{-1} shift (bottom).

The data show a constant average value within error for the peak ratios. This indicates that the fluorescein is in fact volumetrically bound. It is worth noting that the ratio of the two peaks will only be sensitive to thicknesses that fall within the sample depth of the Raman, 2μm. It is possible that the 6A/m^2 film could be above this thickness. The 2 and 4A/m^2 films would not be anywhere near this value and if

the molecule were surface bound it would be seen in a difference between these two ratios at minimum. Since all three show consistent values, it can be assumed that the volume bound case is correct. As mentioned earlier, fluorescein is considered a small molecule, which would make it easy to diffuse through the chitosan film and bind throughout.

The size of the molecule should have an effect on whether the attachment is within the volume or confined to the surface. The identical experiment was repeated using red fluorescent protein. There was no characteristic signal from the RFP detected, therefore only the chitosan signal was measured. Identification of a molecule consistent with a large molecule size, able to bind to chitosan, and with a known Raman signal is necessary to test the size-related behavior of the binding.

4.5 Conclusion

The spatial localization of chitosan electrodeposition and functionalization in the z direction was examined. Fluorescent layer deposition allowed for visualization of the chitosan deposition mechanism, while Raman spectroscopy of NHS-fluorescein provided information as to the binding site for the molecule. It was determined that chitosan deposits in a discrete layer-like behavior. There is however, softening of the boundary edge that occurs between the deposition layers. This is most likely due to the slight dissolution that occurs from the acidic chitosan solution.

As for the location of bound species, the small molecule fluorescein was determined to be volumetrically attached. While it is unclear whether molecules of different sizes will behave in the same manner, the ratio of the fluorescein to chitosan

Raman shifts shows no change with changing thickness, indicating for this size, the attachment occurs throughout the film uniformly.

Chapter 5 : Formation of Chitosan Silver Nanoparticle Composite Films

5.1 Introduction

The versatility of chitosan as a biological interface stems in part from the easily utilized amine ligands present as side groups of the polymer[14]. The hydrogel nature of the polymer provides an additional contribution with a network of porosity providing access to the amine groups in solution as well as a structure to incorporate larger particles. As mentioned earlier, functionalization can occur with the chitosan in solution, on top of the deposited chitosan film, or through the porosity of deposited film. These avenues for functionalization can be used to incorporate silver in four different ways beginning from either ionic or colloidal silver solutions. The incorporated silver was shown to form in a variety of nanostructures that can be used for surface enhanced Raman spectroscopy (SERS) for greatly enhanced sensitivity in identifying chemical species.

The ability for chitosan to chelate metal ions as well as particles is well reported in the literature[20, 45]. Both solid and aqueous chitosan will bind metal ions and particles upon contact. This mechanism can be used to associate chitosan with pre-formed metal particles beginning from a colloidal solution, so that they can be deposited during the chitosan electrodeposition. As mentioned, the chelation mechanism also occurs when the metal is ionic. Aqueous ionic solutions can easily

diffuse through porous materials, enabling the chelation of the metal ion in both chitosan solution and chitosan films.

Other researchers have demonstrated that chitosan can be used to form silver or gold nanoparticles from the respective ionic solution[46-48]. For silver specifically, these studies report the use of chitosan, often times with an added reducing agent, forming silver nanoparticles of varying shapes and sizes[49, 50]. Most studies indicate that through control of solution concentration and temperature, the size of the nanoparticle can be tuned. However, all studies report that chitosan-mediated formation of nanoparticles in solution phase use chitosan solution prepared with acetic acid. These solutions are less desirable for electrodeposition due to a reduction in the free ion concentration, which reduces the conductivity. Our chitosan solution, made from dissolution in HCl and neutralization with NaOH, will also form nanoparticles, but has an additional reaction that occurs between the $AgNO_3$ and the HCl. When free Cl- ions are present, it is known that AgCl will form. The nanoparticles formed in our solutions do not show size dependence based on temperature, but do show a size, density, and morphology dependence based on $AgNO_3$ concentration and reaction time.

5.2 Methods for Composite Film Formation

In all methods for producing composite Ag, chitosan films use either a one or two-step deposition of chitosan and $AgNO_3$ solution as depicted in Figure5.1. Unless noted otherwise the electrodeposition is performed at 3 A/m2 for 2 minutes and

thorough rinsing in phosphate buffer between steps, or deionized water after formation is performed.

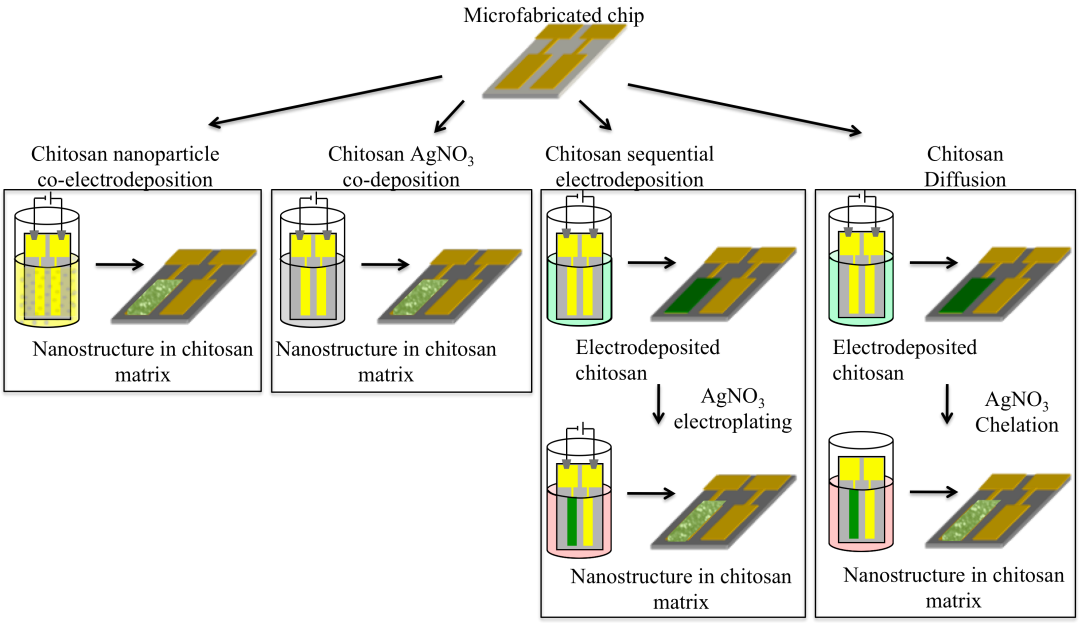

Figure5.1 The four methods for creating chitosan Ag composite films

Nanoparticle co-deposition begins with a colloidal silver suspension. A range of colloidal silver solutions made from 1- 8 mM $AgNO_3$ starting concentrations were used, with the majority of the studies using the 4mM concentration[51]. Colloidal solutions were provided by Seung Yong Lee. The colloidal silver was then mixed with chitosan in varying ratios to obtain the highest particle densities. A 5:1 4mM colloidal silver to 0.5 wt% chitosan solution was used. The chitosan, colloidal silver mixture exhibits the characteristic yellow color of the colloidal silver solution and shows some indication of settling after a 24 hours. Deposition of the mixture is performed identically to deposition of pure chitosan solution.

The other three deposition methods used $AgNO_3$ ionic silver solution in the following range of concentrations; 1, 20, 50, 100, and 150mM. **$AgNO_3$ co-**

deposition is a single step deposition that uses a mixture of $AgNO_3$ and chitosan solutions. These solutions are mixed in a 1:1 ratio. Upon mixing, there is an initial grayish white color change that occurs. Over time, the color will darken and will eventually take on a dark grey/purple color after extended exposure to light. The observed color change is most likely a result of at least part of the $AgNO_3$ reacting with the Cl ions in solution to form AgCl, which is known to be photosensitive. The co-deposition solution is electrodeposited. The voltage during deposition is observed to be lower than that of pure chitosan.

Sequential deposition is a two-step process that uses the chitosan and $AgNO_3$ solutions separately. For this method the chitosan is electrodeposited onto the electrode. The film is then removed from the chitosan solution and rinsed in DI water. The electrode is placed in the $AgNO_3$ solution and deposited at the same current density and time as the chitosan. The voltage readout for the $AgNO_3$ deposition is observed to be around 0.9V and is steady throughout the deposition. This in contrast to the voltage during chitosan deposition, which is 2-3 times greater and increases over time.

The **$AgNO_3$ diffusion** method for film formation is most similar to the sequential deposition in that it is a two-step deposition that uses the pure chitosan and $AgNO_3$ solutions. The process begins by electrodepositing chitosan and rinsing the deposited film. The film is then placed into the $AgNO_3$ solution for 5-10 min. For this method no electric field is applied in the second step. In all cases the chitosan can be removed after composite formation using a mild acid wash. Literature indicates this may partially dissolve the formed silver as well[52]. In the case of the sequential

deposition the removal of the chitosan leaves the electrode with nanostructured silver at the surface.

In all cases the exact chemical reaction in not well known. It is known that ionic Ag will react with ionic Cl. This may be a competing reaction or may be a two-step reaction in which Ag particles are formed from AgCl. In the formation methods that use an applied potential in the Ag deposition step, the electroplating reaction may be contributing as well. In chitosan solution there may also be reaction between the protonated amine and the Ag ion to for Ag particles and nitric acid. Chapter 0shows the three possible reactions.

$$Ag^{+}NO_3^{-} + Na^{+}Cl^{-} + Chit \rightarrow AgCl + NaNO_3 + Chit \quad (1)$$

$$Ag^{+}_{(aq)} + e^{-} \rightarrow Ag_{(s)} \quad (2)$$

$$Ag^{+}NO_3^{-} + Chit\text{-}NH_3^{+} \rightarrow Ag_{(s)} + Chit\text{-}NH_2 + HNO_3 \quad (3)$$

Figure 5.2 Possible reaction occurring in the formation of Ag particles

5.3 TEM characterization of Chitosan Films

TEM samples were prepared by a similar method using an identical deposition technique as the bulk samples. Instead of microfabricated electrodes, amorphous carbon coated gold TEM 200 space grids are used as the substrate. Deposition is done at approximately 2 A/m^2 for 30s, in order to produce films of sufficiently low thickness that electrons can penetrate the sample, ~200 nm. Metrology was performed on a JEOL JEM 2100 TEM equipped with a LaB_6 thermionic emission electron source. EDS analysis was done on this microscope using an Oxford EDS system.

The composite films were created in two phases. The first phase used nanoparticle co-deposition, 1mM co-deposition and 1mM sequential deposition. The intention of phase one was to determine the most efficient method for preparation

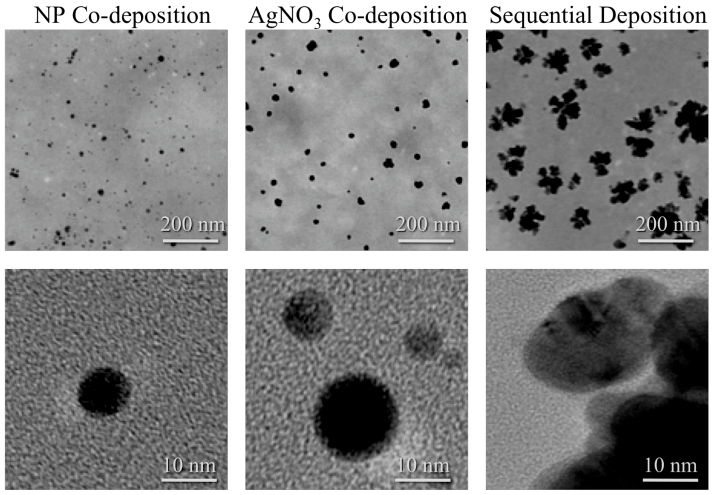

Figure5.3 TEM images from SERS substrate fabrication using nanoparticle co-deposition, 1mM $AgNO_3$ co-deposition and 1mM sequential deposition methods.

of the composite substrates. Figure5.3 clearly shows the striking difference between the two co-deposition methods and the sequential deposition method. The dispersed yet mostly spherical particles in both the nanoparticle and the $AgNO_3$ co-deposition are in sharp contrast to the dense and aggregated structure seen in the sequential deposition.

The intention of the second phase of substrate fabrication was optimizing the substrate for both concentration of $AgNO_3$ as well as the method used. The phase examined the $AgNO_3$ co-deposition, sequential deposition and the diffusion method. The nanoparticle deposition was determined to produce significantly lower particle density than the other two methods in phase one. Three concentrations of $AgNO_3$

solution were used; 1mM, 20mM and 100mM. Figure5.4 shows the TEM formed in each of the substrates.

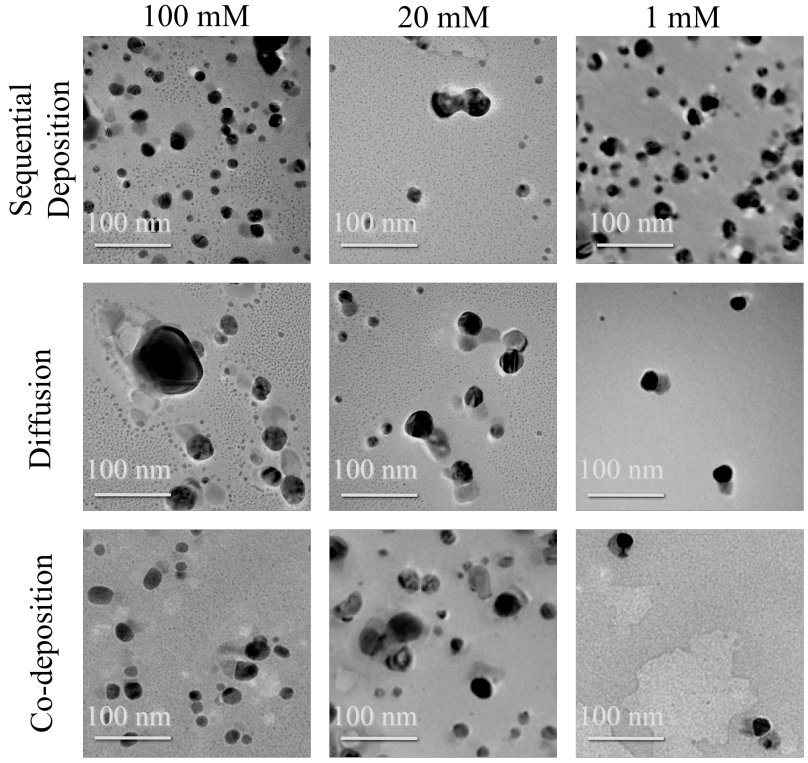

Figure5.4 TEM of the phase two substrates

Initial observation from the TEM results draws few conclusions. It is apparent that the 1mM concentration for diffusion and co-deposition has much lower particle density. The structures of the particles in the co-deposition also appear more uniform than the diffusion and the sequential deposition. Figure5.5 shows the three 100mM concentration samples at two different magnifications. From this, it is clear that the diffusion and sequential deposition have a fine structure, with particles less than 5nm

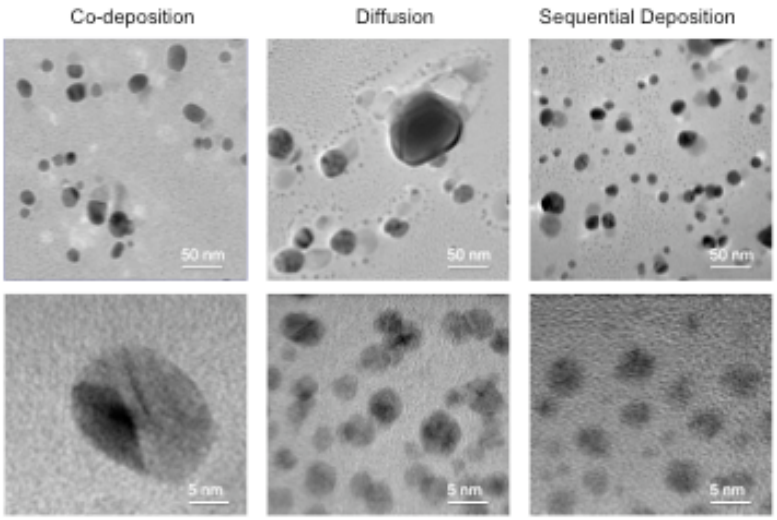

Figure5.5 TEM of substrates produced from 100mM $AgNO_3$

in diameter, that the co-deposition does not. Further magnification of the sequential deposition, as seen in Figure5.6, shows the grain lines associated with crystallinity. To determine the composition of the crystalline particle, EDS analysis is necessary

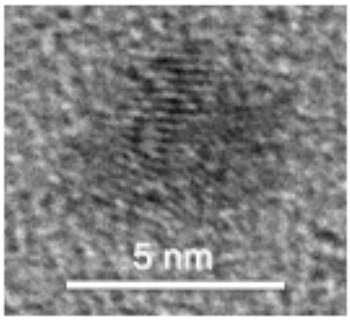

Figure5.6 High magnification TEM of a small particle present in the 100mM sequential deposition

EDS data were taken to confirm the presence of silver in the film. Results from the EDS show Ag and Cl as well as C from the chitosan and grid, and Au from the grid. It is known that the electron beam energy can induce radiolysis, in which the Cl atom will dissociate to leave Ag[53]. This effect is minimized by limiting the exposure of the sample to the beam through use of shutters. Since Cl is present is the scans it is

known that this must not be affecting all of the material in the sample. When the intensity of the EDS spectrum is normalized to the atomic mass of the molecules, it is clear that the Ag contribution is consistently greater than the Cl contribution. If only AgCl was present in the films, the ratio of the two signals would be near 1. Figure5.7 shows the average value of the Ag/Cl ratio for each of the three substrates. The sequential deposition averaged three measurements and had a standard deviation of 0.2. The diffusion and co-deposition both averaged five measurements and had standard deviations of 1.7 and 0.5 respectively.

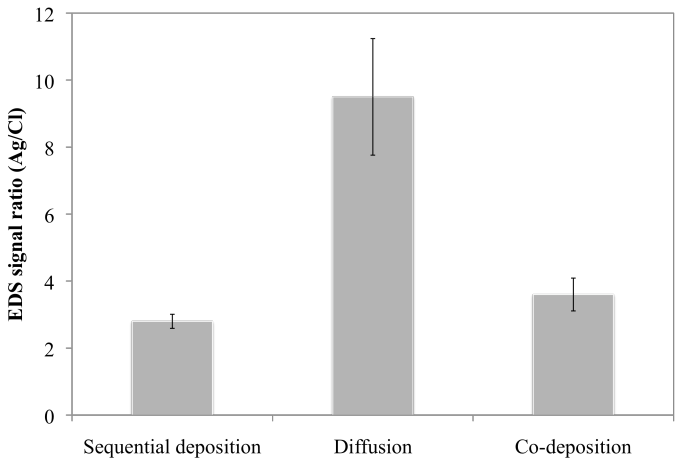

Figure5.7 Ratio of the EDS signal for Ag and Cl

The ratios from the samples where the Ag was electrodeposited are much lower than the diffusion case where no potential is applied. One possible reason for this is that the time that the chitosan is in contact with the $AgNO_3$ solution for the diffusion preparation method is 2 to 5 times longer than it is for the electrodeposition cases. It is known that the Ag and Cl reaction occurs very quickly. It may be that AgCl forms first and that over time, or by addition of energy from a radiation source, that the chitosan further reduces and aggregates the AgCl particles into Ag particles.

Reexamination of Figure5.4 still leaves uncertainty as to the differences between the substrates, particularly between the sequential deposition and diffusion. In order to quantify these images, particle counting via Image J was used. The algorithm for this function counts every high contrast region of a given area, in this case 2nm and above. The area is then converted into diameter by assuming circularity. The scans were then normalized to each other by calculating the number of particles per μm^2. These particle counts were grouped by diameter into four ranges; less than 5 nm, between 5 and 10 nm between 10 and 20 nm and above 20 nm. Analysis was done on one representative image from each formation method over an area of at least 0.6 μm^2 and is shown in the histogram in Figure5.8.

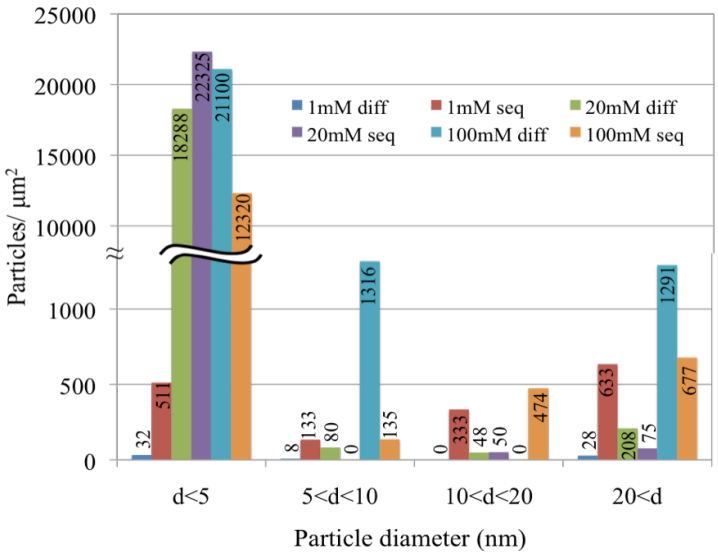

Figure5.8 Histogram of particle sizes present in phase 2 substrates

Initial observation shows the apparent large difference between the small diameter particles in the 1 mM solution versus the other two concentrations. The small particles for the 20 mM and the 100 mM concentrations far outnumber all other

particles in the film. Comparison of the two different formation methods shows that sequential deposition for both 20 mM and 100 mM concentrations have fewer of the largest particles than the diffusion samples. All of the sequential deposition substrates show the lowest particle counts in the 5 to 10 nm range. 10 to 20 nm is the only range which shows the diffusion samples with particle counts than the sequential deposition for a given concentration.

5.4 Analysis of Amine Group Activity in Composite Films

Chitosan was chosen as a material for incorporating Ag nanoparticles, because of the documented use in microfluidics[28]. The primary function of chitosan in microfluidics is to bind biomolecules in a specific location using its amine group functionality. For the composite substrate to be the most versatile, it will possess that ability to form the Ag nanoparticle while maintaining some free amine functionality. In this case, it would potentially allow for attachment of the enzymes directly to the composite substrate, thus localizing the products directly at the site.

The most direct way to test free amine groups existing on the substrate is by exposing a fluorescent molecule to the substrate that will only bind if the amine groups are available. This was done using a penta-tyrosine tagged red fluorescent protein (RFP). The penta-tyrosine (tyr), when reacted with the enzyme tyrosinase, will break off leaving a specifically amine reactive ortho-quinone[24]. Three composite substrates were formed, co-deposition, sequential deposition, and diffusion, at comparable parameters and were immersed in the tyrosinase, tyr-RFP, and buffer solution. The reaction was given 15 minutes to proceed, after which time the chips

were rinsed thoroughly in phosphate buffer and briefly in deionizer water and allowed to dry. While the fluorescence is equally strong in the hydrated films, the time of analysis under the light source will cause drying, leading to inconsistencies in images taken at different times. The dried films were measured with the Zeiss LSM 310 microscope with a TRITC filter. Figure5.9 shows the results form the treatment of the three substrates.

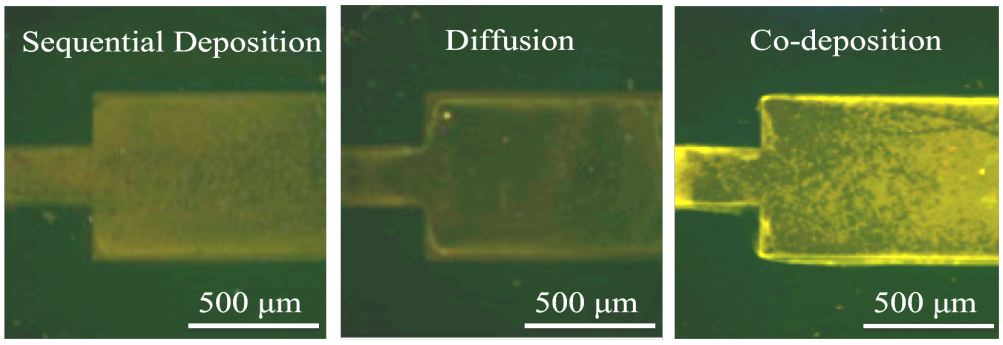

Figure5.9 Fluorescent micrograph of RFP tagged 100mM $AgNO_3$ prepared Ag-chitosan composite substrates

In all cases, noticeable fluorescence is observed, indicating that the chitosan has retained its ability to attach molecules. This result alone indicates the potential of this composite substrate for inclusion into the pre-existing procedures for enzyme immobilization. Each substrate formation method shows differing levels of fluorescence. Since the functionalization and imaging were all performed identically, this indicates the amount of amine availability differs between the methods. Based on that statement it can be said that the co-deposition retains the most activity, the diffusion retains the least, and the sequential deposition is in the middle.

5.5 Discussion

If the analyses of the three techniques used for characterizing the TEM images, EDS Ag/Cl ratio, particle size distribution, and RFP visualized free amine group detection are combined, the following conclusion can be made. The diffusion method of substrate preparation has the most pure silver which, based on particle size distribution, seems to form more large particles relative to the sequential deposition. The diffusion method has the least amine signal based on the RFP binding, indicating that the amine groups are in fact responsible for the Ag particle formation, demonstrating why the RFP signal is the weakest. This may still be related to the processing time. Diffusion time on the order of the electrodeposition times are not sufficient to form the desired structure, so it becomes an inherent limitation of the formation method.

The co-deposition formation method reflects lower particle densities than the other two methods and the highest RFP signal due to amine binding. This would indicate that less of the chitosan is consumed by the particle formation process, but since well dispersed and dense particle formations are desired, this is not a realistic trade-off, making the co-deposition less ideal.

The sequential deposition method reveals the highest Cl ratio, but also shows the highest number of particles in the 10 to 20 nm size range, indicative of strong plasmon enhancement. The higher Cl content may be one reason why there are more active amine sites. It is possible that the electrodeposition of the $AgNO_3$ assists in the formation of the Ag nanoparticle leaving more amine groups free to react elsewhere.

5.6 Conclusions

Between the two phases of substrate formation experiments, initial formation and optimization, it has been demonstrated that there are fours methods for forming nano-structured Ag chitosan films. These films form Ag particles on the order of 2 to 100 nm in diameter. TEM analysis shows that by varying the concentration of the starting ionic $AgNO_3$ solution, different morphologies can be formed.

It has been shown that Ag, and not just AgCl, forms and from the experiments thus far, 100 mM $AgNO_3$ exhibits the highest particle densities. The 100mM $AgNO_3$ sequential deposition substrate is particularly promising in that it shows the highest concentration of particles in the 10 to 20 nm diameter range, reported to be responsible for the greatest level of plasmon enhancement from particles.

Furthermore, the verification of amine group activity of the composite films demonstrates that these films can be used in the same manner as the plain chitosan films. This allows for added functionality in the microfluidic platform without removing any of the characteristics that make chitosan useful as an anchor for these applications.

Chapter 6 : Characterization of Raman Enhancement from Chitosan Composite Substrate

6.1 Introduction

Here the primary intention for incorporating silver into chitosan films is for the detection of the products that result from the AI-2 reaction. Fabrication of the substrate in a manner that is compatible with the microfluidic test bed is important for the eventual integration of this technology. While particle size, density and dispersion are important characteristics of the silver-chitosan composite; ultimately it is the degree of enhancement of a given Raman signal that will indicate whether these substrates are a successful means for signal amplification.

In order to accurately quantify the level of enhancement a given substrate provides, it is important to measure both the base line as well as the enhanced signal. Ideally, the test molecule would be one of the AI-2 reaction products, such as adenine, which is a well-characterized small molecule that is readily available. While the Raman signal for crystalline adenine is quite strong, even concentrated aqueous solutions of adenine show a sharp degradation in signal strength. This low signal makes quantification of a baseline signal more difficult, proving it a non-ideal candidate for substrate optimization. Instead, para-aminothiophenol (PATP), also known as mercaptoaniline, is used as a model analyte. PATP is well documented as a SERS test molecule [54, 55] and shows a relatively strong signal in aqueous solution.

Measurement of enhancement on chips is not sufficient in determining whether a substrate will be a viable option for use as an application based sensor. Analysis of the reproducibility of the measurement and the effect that placing the substrate in a microfluidic system has on the signal are important contributions in determining the effectiveness of the substrate for sensing.

6.2 Measurement of Aminothiophenol Enhancement from SERS substrate

The quantification of Raman enhancement was carried out in two phases, as was done for the TEM metrology. The phase one substrates, nanoparticle co-deposition, 1mM $AgNO_3$ and 1mM sequential deposition, were prepared on 1mm by 8mm electrodes and tested using 1mM of aqueous PATP. All enhancements are measured in reference to the 1145 cm^{-1} Raman shift, a characteristic peak in the PATP signal and calculated by dividing the peak height by the intensity of PATP on a chitosan only substrate.

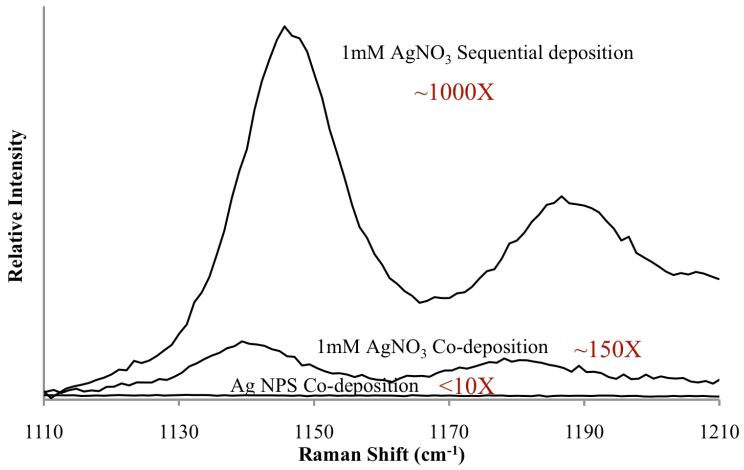

Figure6.1 Raman of PATP signal on phase one substrates

Figure6.1 shows the enhancement differences between the three substrates. All substrates show some enhancement over the background signal; however all three substrates show low enhancement as compared to reported enhancement on the order of 10^5 and greater[34]. The nanoparticle co-deposition has the least enhancement at only 10X. This is not surprising as it had one of the lower particle densities as well. The co-deposition and sequential deposition show corresponding enhancements of 150 and 1000. These are not strong enough enhancers to compete with either naturally formed or fabricated SERS substrates reported in literature, but show promise for the methods as they are the first attempt at fabrication. Measurement of the Raman signal for the phase two optimized substrates is necessary in determining if they show competitive enhancement values.

Phase two substrates have been optimized for both fabrication method and $AgNO_3$. In order to isolate which variable is contributing to the greatest enhancement it is necessary to separate the data obtained from the measurement of PATP in a manner that will isolate the desired information. Figure6.2 shows the Raman spectrum of 100μM PATP for only the 100mM $AgNO_3$ concentration. Arrangement of the data in this manner allows for direct comparison of the three different formation methods with regard to the SERS enhancement. The sequential deposition provides the greatest amount of enhancement.

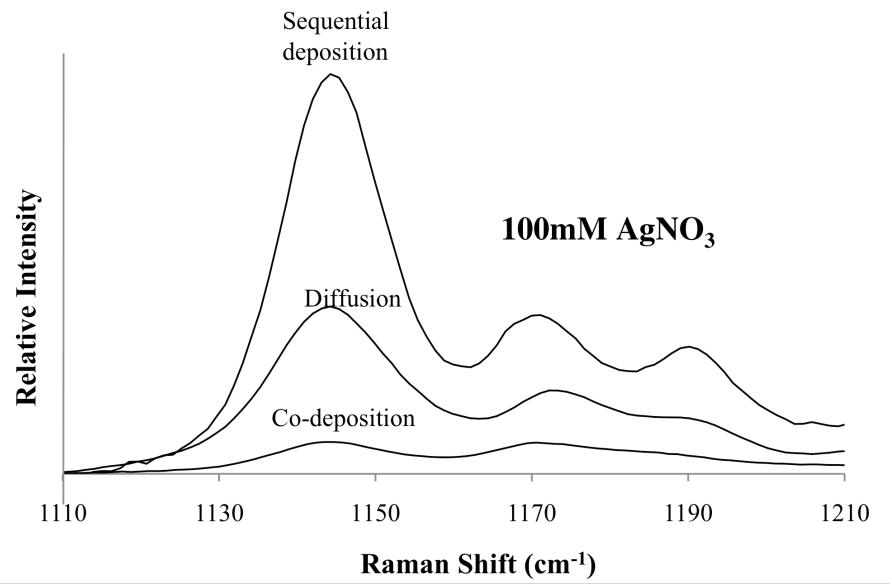

Figure6.2 Relative intensity of PATP from 100mM $AgNO_3$ co-deposition, diffusion and sequential deposition substrate preparation methods.

These findings are consistent with the results from phase one and the findings from chapter 5.4 that indicate it has the greatest particle density in the size range indicated for high SERS enhancement. For this concentration, the three peaks visible in the range 1110 to 1210 cm^{-1} show overall proportionality between the three deposition methods; however, the 1190 cm^{-1} peaks show some slight relative increase. This may be an effect of enhancement or may be an actual change in the vibration characteristic of the sample.

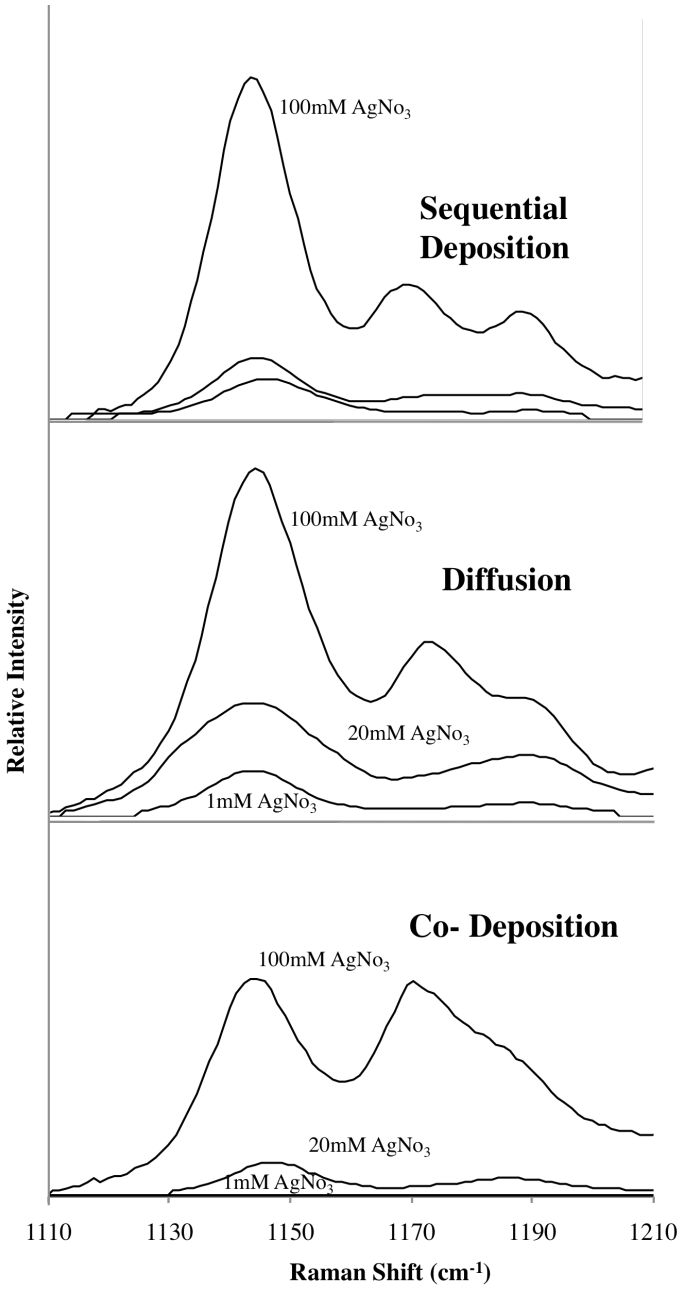

Figure6.3 Effect of AgNO3 concentration of PATP signal strength shown for three of the substrate preparation methods

To isolate the effect of concentration on the PATP enhancement, the spectra were grouped according to the deposition method (Figure6.3). For all three deposition mechanisms increasing $AgNO_3$ concentrations reveals an increase in the enhancement

of the primary 1140 cm^{-1} Raman shift. This figure indicates that of these samples the 100mM sequential deposition is the most effective Raman enhancement substrate. Table 6.1 provides the enhancement value of the primary peak. The corresponding detection limits have been calculated by dividing the enhancement value by the PATP concentration of 100 μM.

Table 6.1 Enhancement values with their corresponding detection limits for the tested substrates

Substrate	SERS enhancement	Detection limit
100mM sequential deposition	42,000X	2 nM
100mM diffusion	17,000X	6 nM
100mM co-deposition	5,000X	20 nM
20mM sequential deposition	10,000X	10 nM
20mM diffusion	8,000X	12 nM
20mM co-deposition	1,000X	100 nM
1mM sequential deposition	7,000X	14 nM
1mM diffusion	3,000X	30 nM
1mM co-deposition	50X	2 μM

Beyond the obvious peak enhancement there is a shift in the relative heights between the three visible peaks in the reported range. The most obvious change is the appearance of the 1170 cm^{-1} peak in the 100 mM concentration in each of the three deposition methods. The peak may also be visible at the 20 mM sequential deposition. The 100 mM co-deposition also shows a difference in the ratio between the 1140 and the 1190 cm^{-1} peaks. Because these peaks appear at higher $AgNO_3$ concentrations, there is a possibility that the substrate is contributing to the signal. To

eliminate this possibility, the signal of the 100mM $AgNO_3$ sequential deposition substrate without the addition of the PATP is taken and compared to the substrate with PATP (Figure6.4)

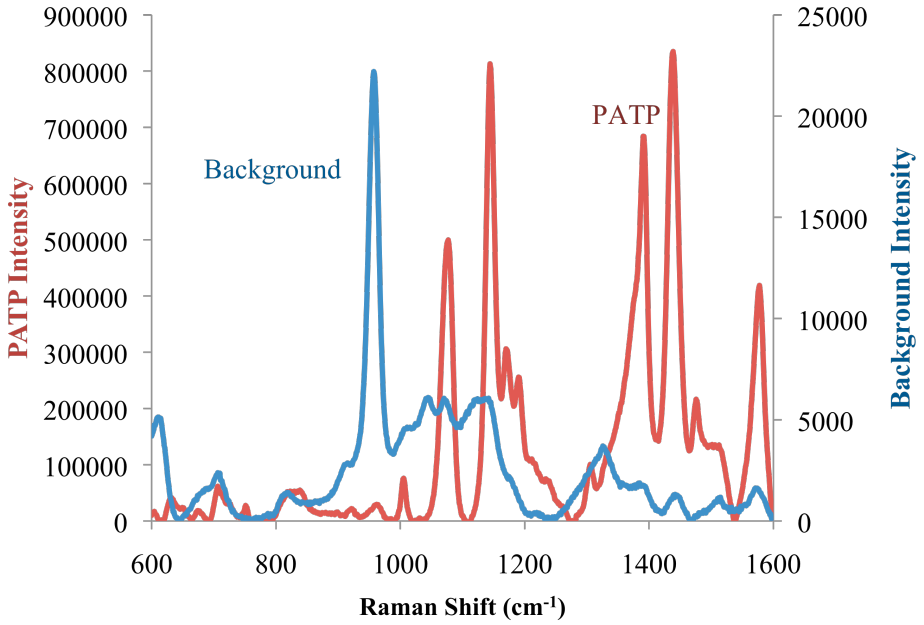

Figure6.4 Raman signal of the substrate, blue, compared to the signal of PATP on the substrate, red.

Comparison of the substrate signal versus the PATP signal shows no overlap in the strong peaks observed. It is also important to note that the intensity scale of the signal from the substrate is about forty times lower. This indicates that any slight overlap between that strong PATP signals and the weak substrate signal are not sufficient to implicate the substrate in the formation of the peak seen at 1170 cm^{-1}. The source of the additional peak must therefore be related to how the PATP interacts with the substrate formed at the higher $AgNO_3$ concentrations.

6.3 Reproducibility of Enhanced Signal

One of the limitations of SERS sensing is the need for "hot spots" in order to measure significant enhancements. According to the literature, hotspots usually occur at the intersection of two particles, or at sharp particle edges[38]. These hotspots contribute to a wide range of enhancements produced from the same substrate, thus producing a lack of reproducibility in the measurement. Particle self-assembly is inherently more random than in the alternative micro and nano fabrication approaches. In order to use this as a potential sensor it is important to have an understanding of the range of signal that can be expected from any given substrate, and whether the hotspots can be located.

The reproducibility of the signal was measured through mapping of PATP on the three most effective substrate preparation methods, the co-deposition, sequential deposition, and diffusion from 100 mM $AgNO_3$ solution. Figure6.5 shows an optical micrograph of the sample including the average Raman intensity and standard deviation. The result is calculated by averaging the data from twenty different physical locations on the rectangular gridded map for a given Raman shift. The standard deviation is also calculated from this data set. For the three substrates, only the sequential deposition shows very clear variation above noise (i.e., clear contrast) in the optical image. The sequential deposition shows the clearest Raman features, with least variability, in the data. Both the co-deposition and the diffusion substrates show standard deviations that exceed the average, indicating variations greater than 100%. The sequential deposition substrate shows a more confined behavior. Initial assessment would lead to the connection between the sequentially deposited

substrates visible microstructure and the improvement in reproducibility, but the points with higher enhancement show no correlation to the observed microstructure in the film. The range of enhancement, maximum divided by minimum, as well as the average percent deviation is shown in Table 6.2.

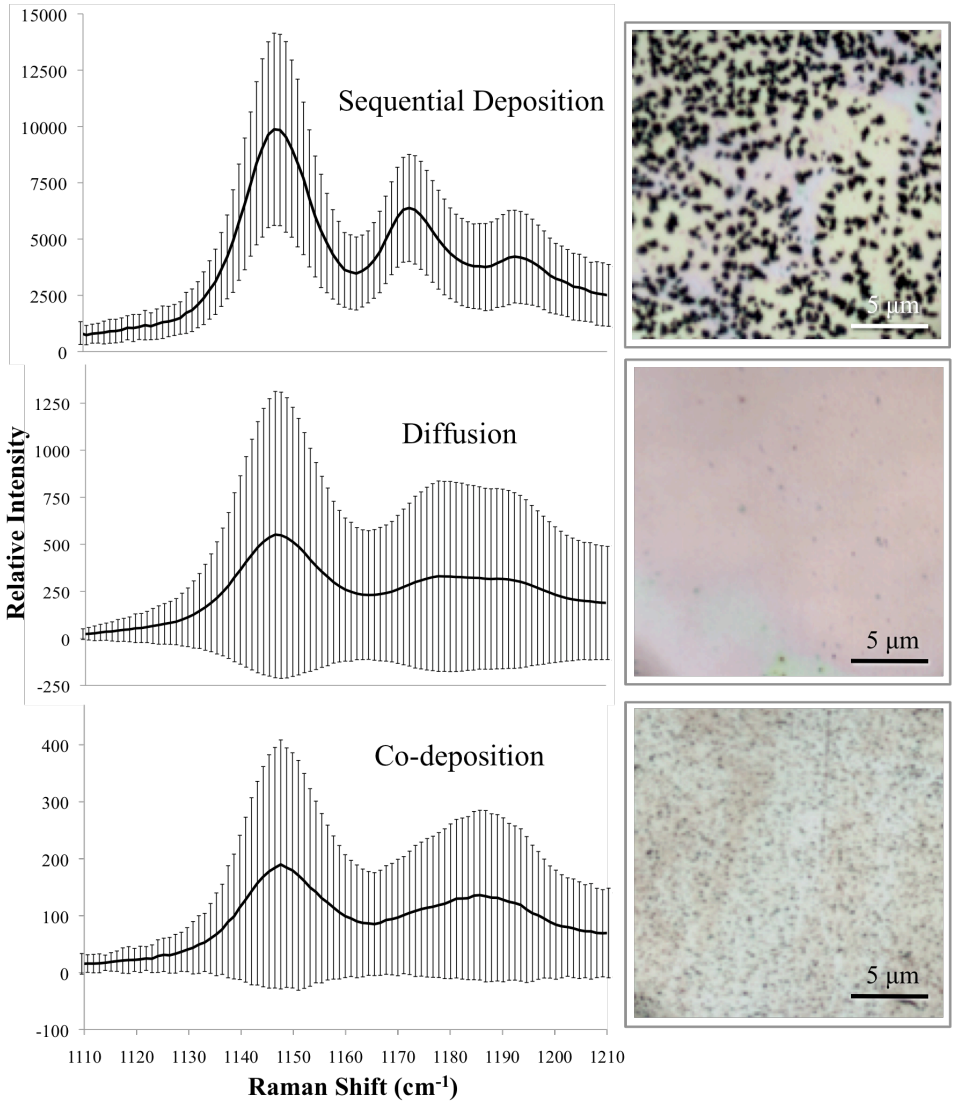

Figure6.5 Average Raman signal and standard deviation of PATP on co-deposition, diffusion and sequential deposition substrates. The corresponding optical micrograph of the substrate is shown to the right of the signal.

Table 6.2 Dependence of enhancement variation on substrate

Substrate	Co-deposition	Diffusion	Sequential deposition
Enhancement range (max/min)	28	298	5
Percent variation (σ/mean)	105%	146%	49%

6.4 SERS Enhancement in Microfluidics

Within a recreated metabolic pathway it is beneficial to enable *in situ* detection of the enzymatic reaction substrate/products so that a real-time measurement of the enzyme conversion can be measured. Since a block in any portion of eth pathway will prevent AI-2 formation, detection of adenine is directly related to whether or not AI-2 has been produced. With pathway recreation now occurring on localized sites in bioMEMS platforms [18, 24, 28], *in situ* detection can be achieved by integrating a SERS substrate into these platforms. The 500-μm-wide, 50-μm-high microchannel with 500 μm X 1000 μm electrode sites is fabricated with negative photoresist SU-8, sealed with PDMS layer and packaged within two Plexiglas plates with a view window above the SERS site. Fabrication of the SERS site follows the phase one sequential deposition method using 1 mM $AgNO_3$ (Figure6.6).

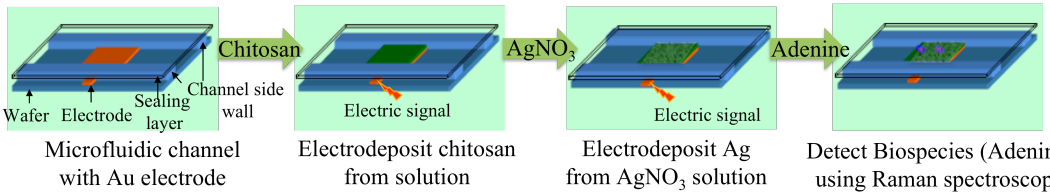

Figure6.6 Creation of SERS site in prefabricated microfluidics bottom is the Raman spectra measured atop the SERS substrate of 1mM adenine in packaged microfluidics. This is compared to spectra from adenine solution at a nanostructured Ag SERS site at the chip level rather than in bioMEMS.

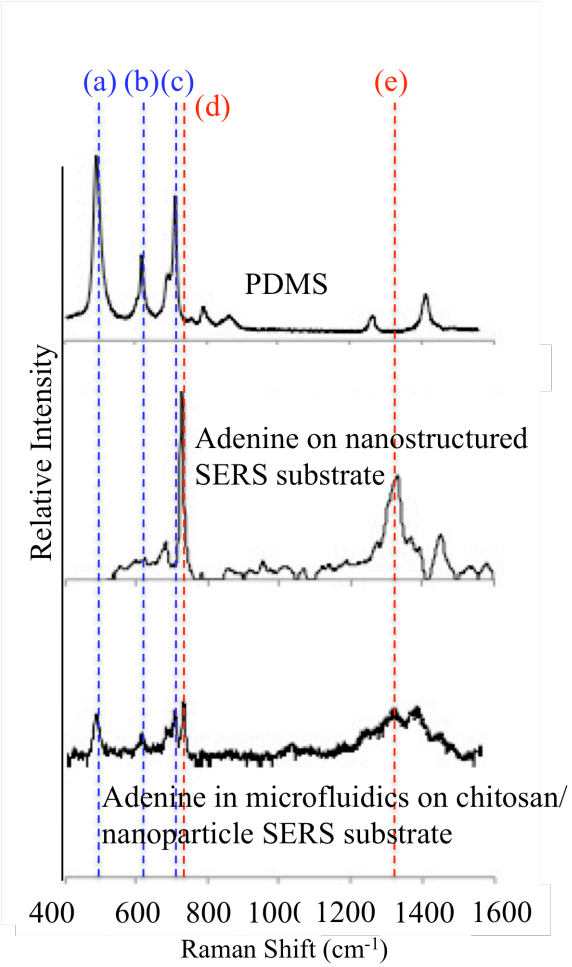

Figure6.7 Raman spectra for PDMS (top), Ag SERS site (middle, no bioMEMS), and adenine at a chitosan/Ag SERS site in bioMEMS, viewed through PDMS (bottom). Peaks a and b and c, 735 and 1327 cm^{-1}, originate from adenine, while d and e are from PDMS.

Adenine in bioMEMS shows its signature 735 cm^{-1} and 1327 cm^{-1} peaks, with the intensity of the former 100X above a non-enhanced signal (Figure6.7). This signal was taken using the 1mM $AgNO_3$ for sequential deposition. The signal shows a 10-fold decrease in intensity versus the equivalent chip-based study. If this indicates the expected reduction of signal through loss from the packaged microfluidic environment, the signal of 10^4 could be expected if the 100 mM sequential deposition were used. Overall, this result demonstrates that our substrates are relevant for detection of products existing in the AI-2 reaction. Moreover, it demonstrates that the signal can be detected through the microfluidics packaging, therefore proving that detection is very possible in our already developed bioMEMS AI-2 reactor.

6.5 Discussion

It is apparent that the sequential deposition substrate shows the greatest enhancement of the PATP signal. It is not clear why that is or why, at greater enhancement, the relative strength of the 1170 cm^{-1} Raman peak increases. As stated, the presence of the 10 to 20nm particles in the greatest concentration most likely is the cause for the increased signal above that of the diffusion sample. If this sample also shows a much greater particle density, it may be this increase in available Ag sites that is contributing to the increase in the smaller signal. It is known that PATP will bind to noble metals such as Ag, via its thiol group. An increase in the density of the particles is a potential cause for a change in the way the PATP binds to the silver. Changes in binding orientation have been shown to contribute to observed vibration shifts. It is also known that the greatest SERS enhancement is obtained when two particles come together to form sharp spaces[25, 38]. If both of these mechanisms are

present this would explain why, with two particles in close proximity, a molecule will shift its orientation due potentially to steric hindrance.

If the increased density in particles is in fact what is causing the increase in signal between the sequential deposition and the diffusion substrates, then it is this density that is allowing for the greater reproducibility seen in the signals. It is interesting to note that the three-fold increase in signal is not proportional to the 60-fold increase in reproducibility. This suggests that more than the increased presence of the 10 to 20 nm particles may affect the reproducibility. For a measurement to be repeatable over different spots, a consistency must be present at the micrometer level. The dramatic increase in the repeatability of the signal indicates that not only are there more of the efficiently sized particles, but the distribution of the electrically deposited particles appears much more uniform than the distribution of the stochastic diffusion-based deposition.

The microfluidics results demonstrate that we may have detection sensitivity down to 100nM. This concentration of adenine falls within the range of what would be expected physiologically, although it is at the upper limit of this range[25]. The laminar flow that exists in microfluidics will be of benefit for detection of the reaction. While overall physiological levels of the adenine present via the AI-2 reaction may be low, if the reaction is produced at the surface of the microchannel, the local concentration may be much greater. This local increase in concentration in the path of a laminar flow regime will be maintained down the channel. The greater concentration in conjunction with the lack of mixing may provide concentrations that will be easily detected in the enzyme-produced reaction.

6.6 Conclusions

Raman characterization of the PATP signal on the chitosan Ag composite substrates demonstrates that the diffusion and the sequential deposition methods for formation provide the greatest amount of SERS enhancement. Based on the reproducibility of the data, the sequential deposition method presents itself as the most viable option for measurement of small molecules in an application environment. The measurement of adenine, in addition to the PATP, demonstrates that the system is relevant for detection of the small molecules present in the AI-2 reaction.

The results from the microfluidics demonstrate the potential for this substrate to be used as an application relevant sensor. Detection via an optimized substrate in the microfluidic channel could be expected to measure concentrations down to 100nM. This sensitivity of measurement should be sufficient when the concepts of local reaction concentration and laminar flow are considered. Overall the Raman characterization of these substrates demonstrates their viability as sensing sites for scientifically relevant applications.

Chapter 7 : Conclusions and Future Work

The work presented builds from previous work demonstrating that chitosan can be electrodeposited and used as a binding interface between microfabricated electrodes and bio molecules. This work has characterized the growth and molecular attachment characteristics of electrodeposited chitosan. Furthermore, it has been demonstrated that chitosan can mediate the formation of Ag nanoparticles via four distinct methods. These substrates have been shown to be viable for SERS based sensing of enzymatic reaction products in microfluidic devices.

Chitosan electrodeposition demonstrates consistent linear growth patterns when observing the instantaneous growth after the initial stages of deposition. The initial stages show less predictable behavior and imply a nucleation mechanism. After initial deposition, chitosan grows in a discrete layer like manner. Above 30s growth time electrodeposition of chitosan is a reliable method of depositing a given thickness at a patterned electrode. Future work in this area should concentrate on characterization of thin films to understand the morphology changes that may be occurring during the first seconds of deposition. Analysis of the pH gradient through solution phase indicators may also provide some insight as to the mechanism of pH dependent growth over time. Furthermore, the in-chamber deposition growth rates show only the first preliminary data of wet film growth measurements. Extension of this work to fully characterize the wet film growth rates for varying current densities and electrode geometries would be useful for optimizing the chitosan growth in microfluidic devices.

Fluorescent and Raman microscopies confirm that the electrodeposition method will deposit chitosan to within 1 μm of the electrode edge. These findings demonstrate that electrodes can be uniquely functionalized if spaced a 2 μm apart. The mechanism for lateral growth is strongly correlated to that of vertical growth. Systematic analysis comparing the thickness and lateral growth, in the as deposited wet and dry films, may provide a definitive ratio of thickness to lateral growth that could provide scaling factors for workable electrode spacings depending on the desired film thickness.

Raman analysis of fluorescein bound to electrodeposited chitosan films indicates the binding for this size of molecule is volumetric. Further work is needed in this area to determine the size relation of this behavior. Measurement of an attached protein or other large molecule should show indications of surface binding. This could be achieved in a qualitative manner by attaching a fluorescent protein in the PDMS growth chamber and observing the extent of fluorescence. A more quantitative study would involve measuring the intensity of a signature Raman peak for a sufficiently large molecule in relation to the chitosan peaks. Quantitative measurement of larger molecules may also show that the amount of surface bound species on chitosan films deposited at different current densities varies with surface roughness and porosity. A result like this would allow for tuning of bound species concentration based on the chitosan deposition parameters.

Chitosan, in addition to utility as an anchor for biomolecules, has shown to be able to mediate the production of Ag nanoparticles. Four fabrication methods have been demonstrated for the production of chitosan/Ag nanocomposite films. Of these

methods diffusion and sequential deposition with $AgNO_3$ solution show the greatest density of particles formed. Through TEM and EDS the particles have been proven to be Ag and show a size distribution. Sequential deposition shows the greatest density of particles in the high enhancing range of 10 to 20 nm. Analysis of the amine group activity in the composite substrates shows availability through the form of tyrosine enabled RFP binding. Overall it has been shown that chitosan can form Ag nanoparticles embedded in an amine active film.

The chitosan/Ag substrates have been shown to be effective SERS enhancers with enhancement values of over 10^5. Characterization of enhancement also indicated the sequential deposition and diffusion are the best substrates with the sequential deposition showing slight improvement comparatively. When the films were analyzed for reproducibility only the sequential deposition showed error within the average range of the data. Based on these two factors the 100mM $AgNO_3$ sequential deposition substrates show promise for use in sensing applications. The 1mM sequential deposition was fabricated in microfluidics and tested on adenine, a product of the AI-2 reaction, and detected 100 μM of adenine. Future work would lend itself to deposition the 100mM sequential deposition substrate in microfluidics for the detection and quantification of adenine. This can be done using purchased adenine for quantification analysis and calibration, and enzymaticaly produced adenine via a multi site reaction in microfluidics. Additional work should also be conducted to determine if the amine binding sites are an effective way to localize reaction products near the Ag nanoparticle to produce SERS enhancement. If amine bound molecules can be sufficiently enhanced, an alternate way to localize products will be available.

This may allow for a more reusable substrate with a wider range of molecules that can be detected and quantified.

Overall I have demonstrated that electrodeposited chitosan has the potential to be a highly reliable way to deposit bio-active substrates. Further work should help to fully understand how the material behaves at all length scales and where molecules of varying sizes will attach, allowing for control of the surface concentration. Chitosan with $AgNO_3$ can easily produce chitosan/Ag nanoparticle substrates that are effective at SERS enhancement sites. These substrates with their amine activity have the potential to create a single site AI-2 reaction pathway with built-in product detection.

Appendices

Appendix I. Procedures

i. Chitosan Solution Preparation

OBJECTIVE: To make 1L 0.5% w/v chitosan solution, pH~5 (scale back accordingly)

NOTE: Chitosan solution is good for about half year. Should make fresh solution twice a year

NOTE:

density of water, rho=0.998g/mL

Dissolving chitosan flakes

1. Weigh 4.99 g chitosan flakes (0.5% w/v)
2. Fill 800mL distilled water in a clean container (~2L) and plate on stirring plate
3. Dump chitosan flakes into distilled water, turn on stirring, monitor with pH meter pH7.0
4. Add dropwise 1M HCl solution using 10mL pipette, wait until stable pH reading before adding next dropwise HCl solution. Track the volume of HCl added.

For example:

1. Add 1st 10mL HCl, pH drops from 7.0 to 5.10
2. After 5 min, add 2nd 10mL HCl, pH drops from 5.10 to 4.60
3. After 5 min, add 3rd 10mL, pH drops from 4.60 to 2.44
4. Cover container with parafilm, leave on stirring plate overnight

NOTE:

i) Best dissolving condition is around pH3, never go below pH 1.0 because final solution will be too salty.

ii) Higher percentage chitosan solution needs longer time, e.g. 2days.

Tuning solution pH ~5

1. pH reading 2.17 after 18 hours, notice solution become obviously viscous with some suspended particles

2. Add dropwise 1N NaOH solution using 5mL pipette, wait until chitosan precipitate dissolved before adding next dropwise NaOH solution. Track volume of NaOH added.

1. Add 1st 1mL NaOH, pH increases from 2.17 to 2.22
2. Add 2nd 1mL NaOH, pH increases from 2.22 to 2.41
3. Add 3rd 1mL NaOH, pH increases from 2.41 to 2.80
4. Add 4th 1mL NaOH, pH increases from 2.80 to 3.41
5. Add 5th 1mL NaOH, pH increases from 3.41 to 4.11
6. Wait for complete dissolving of chitosan precipitate, record pH 4.37 to 4.52

Change to smaller pipette (1mL), add 1N NaOH solution ~0.1mL/droplet

1. Add 0.45 mL NaOH, pH increases from 4.52 to 4.61
2. Add 0.55 mL NaOH, pH increases from 4.61 to 4.79
3. Add 0.20 mL NaOH, pH increases from 4.79 to 4.83
4. Add 0.18 mL NaOH, pH increases from 4.83 to 4.92

Filtrating chitosan solution

1. Add distilled water to bring up to 1L, pH changes from 4.92 to 4.90.

2. Vacuum filtration of chitosan solution twice with "fine" filter 9cm paper, with 2um pore.

3. Store chitosan solution in 4ºC refrigerator. Good for half year.

ii. Fluorescent Dye attachment

NHS-fluorescein or NHS-rhodamine solution was prepared by first dissolving 2.5 mg of NHS-fluorescein in 200 μL of dry dimethylformamide (DMF) and then adding 800 μL of ethanol. The chitosan film was made by adding 50 mL of a 0.4% (w/v) chitosan solution (pH 3.0) to 140 mm diameter Petri dishes. The Petri dishes were oven-dried overnight at 45 °C, and then the dried films were neutralized by immersion in 1 M NaOH for 3-4 h.

After neutralization, the films were washed thoroughly with distilled water and equilibrated with a 0.1 M PBS buffer. This buffer was prepared by dissolving PBS tablets in double distilled H_2O and adjusting the pH to 7.4. The labeling reaction was initiated by adding 20 μL of NHS-fluorescein solution (the DMF/ethanol solution described above) into a Petri dish containing a chitosan film in 35 mL of PBS buffer. After allowing 30 min for reaction, the yellowish-green-colored chitosan films were then rinsed with distilled water and dissolved in a dilute HCl solution (pH ≈ 3). For purification, the fluorescein- labeled chitosan was precipitated by adjusting the pH to about 9 using NaOH. The precipitant was then collected and rinsed with distilled water. After purification the fluorescently labeled chitosan was redissolved in a dilute

HCl solution and the pH was adjusted to 5.0. To determine the polymer concentration, aliquots of known mass were oven-dried, and the residue was weighed[43].

Appendix II. Filter Diagrams

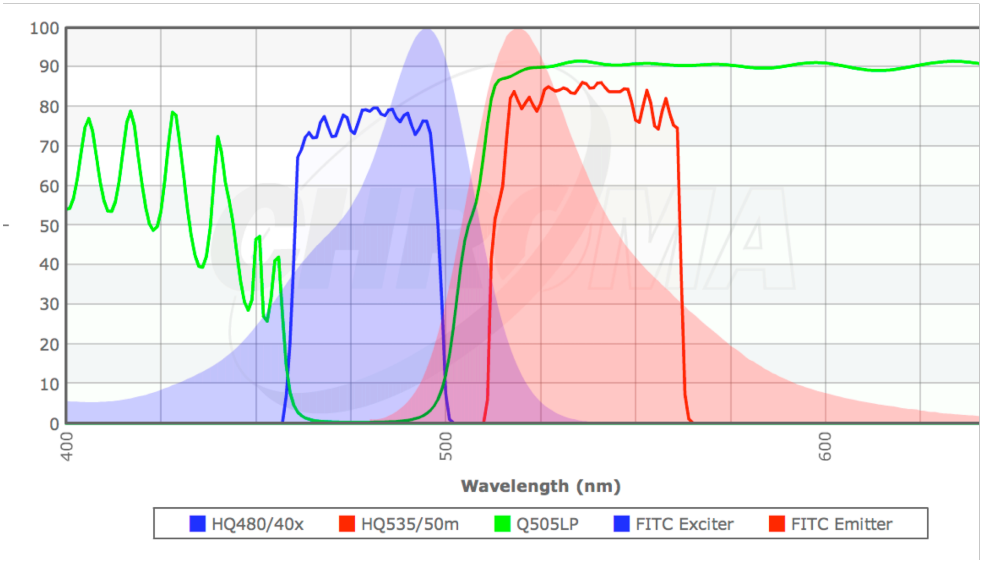

Figure7.1 Band pass diagram for the FITC filter set[56]

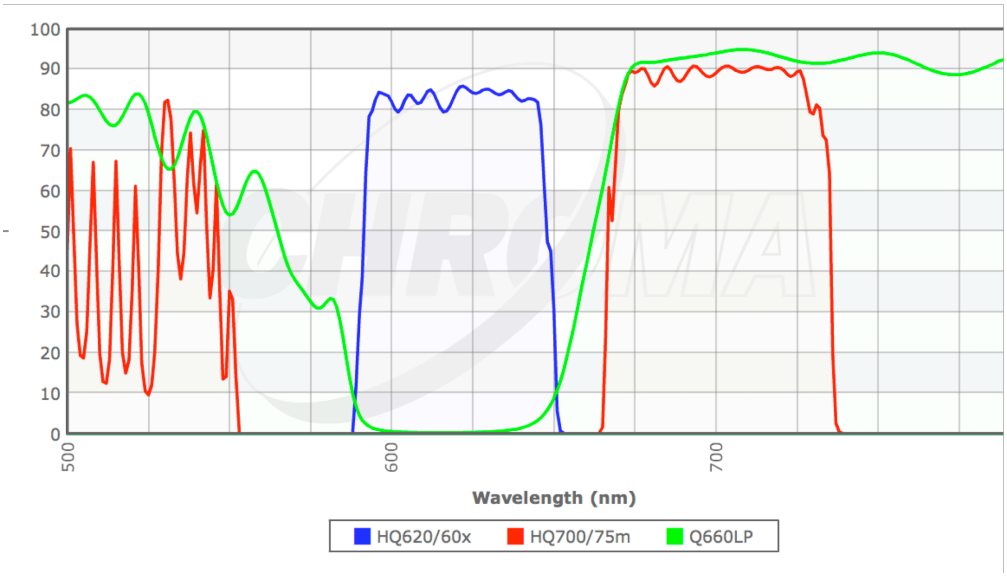

Figure7.2 Band pass diagram for the TRITC filter set[56]

References

1. *J. W. Hong, Y. Chen, W. F. Anderson and S. R. Quake, Journal of Physics-Condensed Matter, 2006, **18**, S691-S701.*
2. *H. Craighead, Nature, 2006, **442**, 387-393.*
3. *E. Verpoorte and N. F. De Rooij, Proceedings of the Ieee, 2003, **91**, 930-953.*
4. *K. K. Jain, Expert Review of Molecular Diagnostics, 2003, **3**, 153-161.*
5. *J. G. E. Gardeniers and A. van den Berg, Analytical and Bioanalytical Chemistry, 2004, **378**, 1700-1703.*
6. *T. Chovan and A. Guttman, Trends in Biotechnology, 2002, **20**, 116-122.*
7. *D. R. Tokachichu and B. Bhushan, Ieee Transactions on Nanotechnology, 2006, **5**, 228-231.*
8. *B. D. Gates, Q. B. Xu, J. C. Love, D. B. Wolfe and G. M. Whitesides, Annual Review of Materials Research, 2004, **34**, 339-372.*
9. *S. Berry, Trends in Biotechnology, 2002, **20**, 3-4.*
10. *J. P. Wikswo, A. Prokop, F. Baudenbacher, D. Cliffel, B. Csukas and M. Velkovsky, Nanobiotechnology, IEE Proceedings -, 2006, **153**, 81-101.*
11. *G. L. Cote, R. M. Lec and M. V. Pishko, Ieee Sensors Journal, 2003, **3**, 251-266.*
12. *H. M. Yi, S. Nisar, S. Y. Lee, M. A. Powers, W. E. Bentley, G. F. Payne, R. Ghodssi, G. W. Rubloff, M. T. Harris and J. N. Culver, Nano Letters, 2005, **5**, 1931-1936.*
13. *K. Salaita, Y. H. Wang and C. A. Mirkin, Nature Nanotechnology, 2007, **2**, 145-155.*
14. *H. S. Kas, Journal of Microencapsulation, 1997, **14**, 689-711.*

15. *L. Q. Wu, A. P. Gadre, H. M. Yi, M. J. Kastantin, G. W. Rubloff, W. E. Bentley, G. F. Payne and R. Ghodssi, Langmuir, 2002,* ***18****, 8620-8625.*

16. *R. A. Zangmeister, J. J. Park, G. W. Rubloff and M. J. Tarlov, Electrochimica Acta, 2006,* ***51****, 5324-5333.*

17. *A. T. Lewandowski, H. M. Yi, X. L. Luo, G. F. Payne, R. Ghodssi, G. W. Rubloff and W. E. Bentley, Biotechnology and Bioengineering, in press.*

18. *J. J. Park, X. L. Luo, H. M. Yi, T. M. Valentine, G. F. Payne, W. E. Bentley, R. Ghodssi and G. W. Rubloff, Lab on a Chip, 2006,* ***6****, 1315-1321.*

19. *H. M. Yi, L. Q. Wu, W. E. Bentley, R. Ghodssi, G. W. Rubloff, J. N. Culver and G. F. Payne, Biomacromolecules, 2005,* ***6****, 2881-2894.*

20. *E. Guibal, Separation and Purification Technology, 2004,* ***38****, 43-74.*

21. *E. J. Soulsby, BMJ, 2005, 2.*

22. *V. Sperandio, A. G. Torres, J. A. Giron and J. B. Kaper, J Bacteriol, 2001,* ***183****, 5187-5197.*

23. *V. Sperandio, A. G. Torres and J. B. Kaper, Mol Microbiol, 2002,* ***43****, 809-821.*

24. *A. T. Lewandowski, D. A. Small, T. H. Chen, G. F. Payne and W. E. Bentley, Biotechnology and Bioengineering, 2006,* ***93****, 1207-1215.*

25. *A. T. Lewandowski, W. E. Bentley, H. M. Yi, G. W. Rubloff, G. F. Payne and R. Ghodssi, Biotechnology Progress, 2008,* ***24****, 1042-1051.*

26. *S. S. Park, H. S. Joo, S. I. Cho, M. S. Kim, Y. K. Kim and B. G. Kim, Biotechnology and Bioprocess Engineering, 2003,* ***8****, 257-262.*

27. *R. Fernandes, C. Y. Tsao, Y. Hashimoto, L. Wang, T. K. Wood, G. F. Payne and W. E. Bentley, Metab Eng, 2007,* ***9****, 228-239.*

28. *X. L. Luo, A. T. Lewandowski, H. M. Yi, G. F. Payne, R. Ghodssi, W. E. Bentley and G. W. Rubloff, Lab on a Chip, 2008, **8**, 420-430.*

29. *H. Mühlpfordt, FluorescenceFilters, http://commons.wikimedia.org/wiki/File:FluorescenceFilters_2008-09-28.svg.*

30. *K. R. Spring and M. W. Davidson, Introduction to fluorescenc microscopy, http://www.microscopyu.com/articles/fluorescence/fluorescenceintro.html, 2009.*

31. *E. Smith and G. Dent, Modern Raman Spectroscopy - A Practical Approach, John Wiley& Sons Ltd, West Sussex, England, 2006.*

32. *J. B. Pendry, A. J. Holden, W. J. Stewart and I. Youngs, Physical Review Letters, 1996, **76**, 4773-4776.*

33. *K. A. Willets and R. P. Van Duyne, Annual Review of Physical Chemistry, 2007, **58**, 267-297.*

34. *K. Hering, D. Cialla, K. Ackermann, T. Dorfer, R. Moller, H. Schneidewind, R. Mattheis, W. Fritzsche, P. Rosch and J. Popp, Analytical and Bioanalytical Chemistry, 2008, **390**, 113-124.*

35. *G. A. Baker and D. S. Moore, Analytical and Bioanalytical Chemistry, 2005, **382**, 1751-1770.*

36. *R. A. Tripp, R. A. Dluhy and Y. P. Zhao, Nano Today, 2008, **3**, 31-37.*

37. *A. Otto, I. Mrozek, H. Grabhorn and W. Akemann, Journal of Physics-Condensed Matter, 1992, **4**, 1143-1212.*

38. *G. L. Liu, Y. Lu, J. Kim, J. C. Doll and L. P. Lee, Advanced Materials, 2005, **17**, 2683-+.*

39. *S. L. Buckhout-White and R. Gary W, Sift Matter, 2009.*

40. *P. C. Chen, R. L. C. Chen, T. J. Cheng and G. Wittstock, Electroanalysis, 2009, **21**, 804-810.*

41. *H. C. Wu, X. W. Shi, C. Y. Tsao, A. T. Lewandowski, R. Fernandes, C. W. Hung, P. DeShong, E. Kobatake, J. J. Valdes, G. F. Payne and W. E. Bentley, Biotechnology and Bioengineering, 2009, **103**, 231-240.*

42. *A. Di Martino, M. Sittinger and M. V. Risbud, Biomaterials, 2005, **26**, 5983-5990.*

43. *L. Q. Wu, H. M. Yi, S. Li, G. W. Rubloff, W. E. Bentley, R. Ghodssi and G. F. Payne, Langmuir, 2003, **19**, 519-524.*

44. *R. Fernandes, L. Q. Wu, T. H. Chen, H. M. Yi, G. W. Rubloff, R. Ghodssi, W. E. Bentley and G. F. Payne, Langmuir, 2003, **19**, 4058-4062.*

45. *P. R. Stoddart, P. J. Cadusch, T. M. Boyce, R. M. Erasmus and J. D. Comins, Nanotechnology, 2006, **17**, 680-686.*

46. *D. S. dos Santos, P. J. G. Goulet, N. P. W. Pieczonka, O. N. Oliveira and R. F. Aroca, Langmuir, 2004, **20**, 10273-10277.*

47. *X. H. Guo, D. Zheng and N. F. Hu, Journal of Physical Chemistry B, 2008, **112**, 15513-15520.*

48. *D. W. Wei and W. P. Qian, Colloids and Surfaces B-Biointerfaces, 2008, **62**, 136-142.*

49. *D. W. Wei, W. P. Qian, D. J. Wu, Y. Xia and X. J. Liu, Journal of Nanoscience and Nanotechnology, 2009, **9**, 2566-2573.*

50. *A. Murugadoss, P. Goswami, A. Paul and A. Chattopadhyay, Journal of Molecular Catalysis a-Chemical, 2009, **304**, 153-158.*

51. *S. D. Solomon, M. Bahadory, A. V. Jeyarasingam, S. A. Rutowsky, C. Boritz and L. Mulfinger, Journal of Chemical Education, 2007,* ***84****, 3.*

52. *Y. Lu, Q. Wang, J. Sun and J. Shen, Langmuir, 2005,* ***21****, 5179-5184.*

53. *D. B. Williams and C. B. Carter, in Transmission Electron Microscopy, Springer, New York, Editon edn., 2009.*

54. *Y. J. Sun, L. Wang, L. L. Sun, C. L. Guo, T. Yang, Z. L. Liu, F. G. Xu and Z. Li, Journal of Chemical Physics, 2008,* ***128****, -.*

55. *H. Y. Koo, W. S. Choi, J. H. Park and D. Y. Kim, Macromolecular Rapid Communications, 2008,* ***29****, 520-524.*

56. *http://www.chroma.com/products/catalog/31000_Series/31002.*